Title: Preoptic Neurons that Control Entry into Hibernation

Authors: Adrian J. Martinez[1,2]†, Christopher M. Reid[1]†, Aurora J. Lavin-Peter[1], Wenhui Li[1], Andrew S. Lee[1], Eric C. Griffith[3], Sinisa Hrvatin[1,4,5*]

Affiliations:

[1]Whitehead Institute for Biomedical Research, Cambridge, MA 02142, USA

[2]Department of Brain and Cognitive Sciences, Massachusetts Institute of Technology, Cambridge, MA 02142, USA

[3]Department of Neurobiology, Harvard Medical School, Boston, MA 02115, USA

[4]Department of Biology, Massachusetts Institute of Technology, Cambridge, MA 02142, USA

[5]Howard Hughes Medical Institute, Massachusetts Institute of Technology, Cambridge, MA, USA

*Corresponding author. Email shrvatin@wi.mit.edu (S.H.)

† These authors contributed equally to this work

Abstract: Evolution of seasonal hibernation has enabled mammals to survive harsh conditions by entering a state of prolonged hypometabolism and hypothermia with body temperatures as low as 0-4°C[1–6]. Despite decades of physiological studies, the genetic tools to study hibernation have remained limited and the mechanisms that induce hibernation entry are still unknown. Focusing on the brain, we map state-dependent neuronal activity across the hibernation cycle in Syrian hamsters and identify the hypothalamic anterior preoptic area (aPOA) as a key regulator of hibernation entry. Single-nucleus RNA and chromatin profiling provided a map of neuronal populations present in the hamster POA and enabled the discovery and design of an enhancer AAV that selectively targets hibernation-associated aPOA subpopulations. Using this genetic approach, we show that *Samd3*-positive aPOA glutamatergic neurons are necessary for entry into hibernation and that their activation is sufficient to induce a prolonged hypothermic state with associated nesting behavior. Together, we identify the first neuronal population that controls entry into hibernation, opening new avenues for investigating and manipulating the metabolic and physiological mechanisms underlying this extreme state of “suspended animation” and its potential applications in aging and disease.

Main Text: Maintaining core body temperature (T_b) within a narrow range is a defining feature of warm-blooded animals[7,8]. Yet, to survive in extreme environments, many birds and mammals, including some primates, have evolved the ability to initiate hibernation, a state associated with profound reductions in heart rate, respiration, metabolic rate, and core body temperature—sometimes reaching as low as 0-4°C[1–6]. How warm-blooded animals initiate such extreme hypometabolic states and how their cells survive at these low temperatures have long remained fundamental questions in homeotherm biology. Moreover, an understanding of the mechanisms controlling hibernation could have important medical applications from therapeutic hypothermia and organ preservation to prevention of muscle atrophy, aging, and potentially even space travel[9–20].

The defining feature of hibernation is a controlled reduction of metabolic rate, yet hibernation is regulated and expressed in distinct ways across species[2,3]. Large hibernators, such as bears, maintain a relatively constant T_b near 30-36°C[21], whereas hibernating rodents like the arctic ground squirrels decrease T_b to below 0°C[6]. Animals in moderate and cold climates typically hibernate during winter, while tropical hibernators, such as lemurs, hibernate in the dry warm season[3,22]. Given the phenotypic differences and breadth of animals capable of hibernation, it remains unclear to what extent the underlying mechanisms regulating hibernation are conserved across species.

The search for the triggers of hibernation entry is long-standing, with multiple models having been proposed, including the existence of circulating hibernation-inducing factors[23–26]. More recently, advances in neuroscience have enabled detailed mapping of the core brain–body thermoregulatory circuits[7,8,27–38] and have identified hypothalamic neuronal populations in mice that regulate fasting-induced daily torpor[39–44]. However,

these studies were conducted in non-hibernating species and the extent to which homologous circuits evolved to regulate seasonal hibernation has yet to be determined. Moreover, the lack of genetic access in hibernators has thus far prevented the identification, dissection, and manipulation of brain circuits that regulate seasonal hibernation. As a result, although multiple environmental cues and hormonal systems are known to modulate hibernation timing and depth in different species[1,45–57], which neuronal populations control entry into hibernation has remained unknown.

To probe the neural mechanisms that control entry into hibernation, we established a laboratory paradigm of hibernation in the Syrian hamster (*Mesocricetus auratus*). In these animals, hibernation is defined by repeated bouts of profoundly decreased metabolic rate and body temperature called *deep torpor* (DT) punctuated by brief arousals that restore normal body temperature referred to as interbout euthermia (IBE)[2,6,58–61]. To monitor entry into DT, we implanted each animal with telemetric temperature probes. To induce hibernation, adult (5-6-week-old) animals housed at room temperature (~22ºC) with standard photoperiod (12 hours light (L): 12 hours dark (D)) were first shifted to a short photoperiod (8L:16D) for 8-10 weeks, followed by transfer to 4-5°C ambient temperature conditions to simulate seasonal changes (Fig. 1a, b, Extended Data Fig. 1a). While this paradigm induced hibernation in both males and females, female hamsters were initially found to hibernate more readily (data not shown), with ~80% initiating torpor bouts within six weeks of ambient temperature reduction. As a result, we restricted our subsequent analyses to females.

While typical torpor-associated T_b decreases followed an exponential decay curve (n = 1262 torpor bouts, Extended Data Fig. 1b), animals exhibited some variability in torpor

80 dynamics. Altogether, 69% of animals (n = 271) achieved DT (minimal T_b = 5.5 ± 0.5°C,
81 bout duration 60.3 ± 13.4 h) and 11% (n = 42) exhibited only shallow torpor bouts (minimal
82 T_b = 12.2 ± 3.1°C, bout duration 6.8 ± 1.8 h), with 20% (n = 81) failing to initiate torpor
83 during the 6-week observation period (Fig. 1c-f, Extended Data Fig. 1c). Periods of IBE
84 between DT bouts lasted 15.3 ± 2.8 h (n = 2471 IBE periods, Fig. 1e). Moreover,
85 consistent with prior reports[62], torpor entry occurred preferentially during subjective night
86 (~ZT17-18) (n = 3,595 torpor bouts, Fig. 1g) and was characterized by a stereotyped
87 nesting behavior with curled posture and absence of gross motor movement, food, or
88 water intake[2,61]. By contrast, arousal from DT exhibited no clear circadian pattern (Fig.
89 1h), consonant with disrupted circadian clock oscillations at temperatures below
90 15°C[62,63].

91

92 **POA activity regulates hamster entry into deep torpor**

93 Having established laboratory conditions for efficient hibernation induction, we
94 employed this system to investigate neural activity changes associated with DT onset. To
95 this end, we collected brain samples during DT and IBE, as well as from non-hibernating
96 control animals, and performed immunostaining for FOS, a marker of neuronal activity
97 (Fig. 2a). Given prior reports of neuronal activity marker induction in hypothalamic regions
98 during DT bouts[39,62,64], and classic studies showing that hypothalamic lesions disrupt T_b
99 regulation during hibernation[65], we focused our analysis primarily on the hypothalamus.
100 Among the 32 distinct regions analyzed, we observed DT-active regions associated with
101 circadian rhythm modulation (Suprachiasmatic nucleus)[66–68], energy homeostasis
102 (Arcuate nucleus)[69–71], and arousal (Paraventricular nucleus of the thalamus)[72,73].

103 Notably, the anteroventral periventricular nucleus (AVPe) within the anterior POA
104 exhibited the highest degree of FOS induction in DT relative to IBE or non-hibernating
105 control samples (14.1% vs. 6.9% and 0.8%, $P = 0.0685$ and $P < 0.001$, respectively) (Fig.
106 2b-d, Supplementary Tables 1, 2, Extended Data Fig. 2a, b).

107 To test directly whether hypothalamic neuronal activity is required for the initiation and
108 maintenance of hibernation, we stereotaxically injected adeno-associated virus (AAV)
109 expressing an inhibitory Gi-coupled DREADD (Designer Receptor Exclusively Activated
110 by Designer Drug; AAV-hSyn-hM4D(Gi)-mCherry)[74] into hibernating hamsters (Fig. 2e),
111 systematically targeting different areas of the anterior hypothalamus that exhibited
112 substantial DT-associated activity. After allowing animals to recover and resume DT
113 bouts, we administered the DREADD agonist clozapine (CLZ) via drinking water. As
114 animals consumed CLZ during their IBE periods, we observed a cessation of torpor bouts
115 in a subset (4/13) of the tested animals, while all animals that underwent sham surgery
116 and received CLZ (5/5) readily re-entered torpor (Fig. 2f-h, Extended Data Fig. 2c).
117 Correlation of the pattern of Gi-DREADD expression across animals with the degree of
118 DT perturbation identified subregions of the anterior POA (aPOA), including the medial
119 preoptic area (MPO), medial preoptic nucleus (MPN), and AVPe, as regions whose
120 silencing was associated with perturbed hibernation (Fig. 2h-j, Supplementary Table 3).
121 Together, these findings implicate the anterior preoptic area as a key region whose
122 activity is necessary for the initiation of DT bouts during hibernation.

123

124 **Cross-species transcriptomic profiling identifies DT-active neuronal populations**

125 The aPOA has been implicated in the regulation of fasting-induced daily torpor (FIT)
126 in mice[39–44]. Our chemogenetic silencing studies in hamster therefore raised the
127 possibility that this region plays a conserved role in the control of hypometabolic states
128 across mammals. To gain further insight into the diversity of neural cell types in the
129 hamster POA and their relation to the cellular composition of the murine POA, we
130 dissected and profiled the POA of 7 adult hamsters (4 females and 3 males) using single-
131 nucleus paired RNA- and ATAC- sequencing (multiome) (Fig. 3a). We annotated the
132 hamster POA cells by aligning and integrating the resulting data with recently published
133 mouse POA multiome and spatial transcriptomic datasets[75,76], generating the first
134 multiomic cross-species POA cellular taxonomy (Extended Data Fig. 3-5).

135 Since activity of brain regions within the median and medial POA was essential for DT
136 entry (Fig. 2i), we focused our analysis on these regions. Graph-based clustering
137 identified major neuronal and non-neuronal cell classes, with further subclustering of
138 neuronal cells (*n* = 26,761 cells) identifying 15 distinct GABAergic and 11 glutamatergic
139 neuronal cell types shared between hamster and mouse (Fig. 3b-d, Extended Data
140 Fig. 4). Importantly, every neuronal cluster contained both mouse and hamster cells (Fig.
141 3c), and pair-wise transcriptional similarity analysis (cosine similarity score) between all
142 hamster and murine neuronal cell clusters revealed consistent 1:1 cross-species
143 relationships, further supporting the validity of our cross-species atlas alignment (Fig. 3e).
144 Moreover, with the exception of a few cell types, the relative cell type abundance across
145 POA neuronal clusters was largely preserved between hamster and mouse (Extended
146 Data Fig. 5e). Thus, our analyses reveal broad cellular homology between hamster and
147 mouse POA.

148 Focusing more closely on POA neuronal populations implicated in FIT in the mouse,
149 we found that the expression patterns of molecular markers of mouse FIT-associated
150 neurons (*Slc17a6/Vglut2, Adcyap1, Esr1,* and *Ptger3*) were broadly conserved across
151 hamster and mouse POA cell types (Fig. 3f, g). Moreover, *in situ* hybridization (ISH)
152 analysis indicated that *Vglut2* and *Adcyap1*, two broad markers of FIT-regulating cells,
153 labeled neurons in similar anatomical locations in the mouse and hamster aPOA,
154 including the AVPe, MPO, and MnPO (animals = 4, Fig. 3h, Extended Data Fig. 6).
155 Leveraging these findings, we carried out combined immunostaining and ISH on aPOA
156 samples from hamsters (n = 3) in deep torpor and found that the majority of DT-active
157 (FOS-positive) neurons express *Slc17a6/Vglut2* (65.2 ± 4.2%, animals = 3), with a
158 considerable portion expressing *Adcyap1* (34.0 ± 1.4%, animals = 3), and relatively few
159 expressing *Slc32a1/Vgat* (12.8 ± 1.5%, animals = 3, Fig. 3i, j, Extended Data Fig. 7a, b).
160 Together, these findings suggest that homologous aPOA glutamatergic neuronal
161 populations may be active during mouse FIT and hamster DT.

162 To further test this idea, we leveraged anatomical information from our transcriptomic
163 and anatomical atlas to identify Glut-04, -06, -07, -09, -10, and -11 clusters as
164 corresponding to FIT-regulating neurons (hereafter collectively termed $aPOA^{Vglut2}$
165 neurons; Fig. 3k, Extended Data Fig. 7c), and expression of the *Samd3* gene was found
166 to exclusively mark this population (Fig. 3l). Indeed, a substantial fraction of hamster DT-
167 active (FOS+) neurons also expressed *Samd3* (46.4 ± 4.1% of FOS+ AVPe neurons are
168 positive for *Samd3* mRNA, Fig. 3m, n), further supporting the idea that $aPOA^{Vglut2}$ neurons
169 are active during DT entry and might regulate entry into this state. Together, our findings
170 establish the first cross-species atlas of the aPOA, a key region whose activity is

171 necessary for the initiation of DT bouts during hibernation, uncovering broad homology
172 between mouse and hamster cell types and implicating aPOA^{Vglut2} neurons as promising
173 candidate drivers of DT entry in the hamster.

174

175 **Enhancer-driven viral tools to access aPOA^{Vglut2} neurons**

176 To assess the functional role of aPOA^{Vglut2} neurons in hamster DT entry, we required
177 the ability to selectively target and manipulate these cell populations *in vivo*. Transgenic
178 options in the hamster remain limited, and a *CamkIIa* promoter-driven AAV exhibits poor
179 specificity for glutamatergic neurons in the hamster POA (42.6 ± 2.0%, animals = 4,
180 Extended Data Fig. 8). Recently, AAV constructs incorporating compact cell-type-specific
181 enhancer gene regulatory elements (GREs) have offered a promising alternative to
182 traditional transgenic technologies in nonstandard species[77–83]. We therefore sought to
183 generate new enhancer-AAV tools driving restricted payload expression in the target
184 aPOA^{Vglut2} cell population.

185 To develop a viral approach to selectively target aPOA^{Vglut2} neurons, we leveraged the
186 extensive murine single-nucleus chromatin accessibility (snATAC-seq) data included in
187 our multiomic cross-species atlas to identify conserved genomic elements exhibiting
188 selectively enhanced accessibility in aPOA^{Vglut2} neuron cell populations (Fig. 4a). First,
189 we employed a modeling-based approach to identify cell-type-specific nucleosome-
190 depleted gene regulatory regions. Subsequently, we performed differential accessibility
191 analysis to identify putative GREs with enriched accessibility in aPOA^{Vglut2} neuronal
192 populations relative to other neuronal subtypes (Fig. 4b, Extended Data Fig. 9), and
193 filtered GREs based on proximity to aPOA^{Vglut2} neuron-restricted marker genes (Fig. 4c).

194 Notably, using this approach, we identified a conserved 500 bp element proximal to the
195 mouse *Samd3* gene, hereafter termed *Samd3E*, that exhibited the highest accessibility
196 enrichment in aPOA^{Vglut2} neurons relative to caudal POA^{Vglut2} neurons and POA^{Vgat}
197 neurons (FDR < 10^{-300}, log_2Fold Enrichment = 3.1, Fig. 4b-e), with similar aPOA^{Vglut2}
198 neuron-enriched accessibility also observed in the hamster (P = 10^{-173}, log_2Fold
199 Enrichment versus other populations = 3.2, Fig. 4f, Extended Data Fig. 9).

200 The resulting candidate mouse GRE sequences were synthesized and cloned into an
201 AAV backbone upstream of a minimal beta-globin promoter sequence and a red
202 fluorescent protein (RFP) reporter transgene prior to packaging into functional AAV8
203 particles for *in vivo* evaluation. Notably, the *Samd3E* element conferred remarkable
204 specificity, restricting reporter expression almost exclusively to *Vglut2*+ neurons in the
205 hamster aPOA (95.2 ± 1.2%; animals = 3), with substantial co-labeling of *Samd3*+ cells
206 (58.7 ± 3.2%, animals = 3, Fig. 4g, h, Extended Data Fig. 10). Taken together, these
207 findings highlight the power of this approach to generate viral tools to study brain circuits
208 across species, including in hibernating animals, and establish the *Samd3E*-driven AAV
209 (Samd3E-AAV) as an effective tool for achieving targeted genetic access to glutamatergic
210 neurons of the anterior POA.

211

212 **aPOA^{Vglut2} neuronal activity is necessary and sufficient for deep torpor entry**

213 Employing our newly developed Samd3E-AAV, we set out to address the role of
214 aPOA^{Vglut2} neuronal activity in hibernation and DT by expressing an inhibitory Gi-
215 DREADD (AAV-Samd3E-hM4D(Gi)-EGFP) in hamster aPOA^{Vglut2} neurons (Fig. 5a).
216 Neuronal inhibition via CLZ administration had no significant effect on basal homeostatic

217 T_b or circadian T_b rhythmicity in control non-hibernating Gi-DREADD-expressing
218 hamsters (Extended Data Fig. 11a, b). However, actively hibernating Gi-DREADD-
219 expressing (n = 12) animals showed a significant delay in the resumption of DT bouts
220 following CLZ treatment compared to when these same animals were administered a
221 water-only vehicle control (114.9 ± 45.4 hours vs. 64.1 ± 24.5 hours, P = 0.0003). Indeed,
222 a majority (7/12) of CLZ-treated Gi-DREADD-expressing animals failed to re-enter DT
223 during the full 6-day course of CLZ treatment, whereas none (0/12) of the animals failed
224 to resume DT during treatment with the vehicle control. Moreover, animals (n = 5)
225 expressing a control reporter payload (AAV-Samd3E-EGFP-Synaptophysin-mRuby)
226 exhibited no significant difference in the time to DT resumption following CLZ or vehicle
227 treatment (61.6 ± 26.5 hours vs. 47.4 ± 10.2 hours, respectively. P = 0.6167), with all
228 animals resuming torpor bouts within the CLZ treatment window (Fig. 5b, c). Together,
229 these results strongly suggest that $aPOA^{Vglut2}$ neuronal activity is required for entry into
230 hibernation-associated DT.

231 To determine the extent to which $aPOA^{Vglut2}$ neuron activity is sufficient to drive DT
232 entry, we selectively introduced an excitatory Gq-DREADD into hamster $aPOA^{Vglut2}$
233 neurons via our Samd3E-AAV (AAV-Samd3E-hM3D(Gq)-EGFP, Fig. 5d). CLZ
234 administration led to a rapid, significant drop in T_b in Gq-DREADD-expressing hamsters,
235 with the animals reaching a minimum body temperature of 13.9 ± 1.0ºC (P < 0.0001
236 relative to normothermia) and maintaining a reduced body temperature for 56.9 ± 13.1
237 hours, consistent with the induction of a prolonged torpor-like state (Fig. 5e-g). By
238 contrast, these same animals exhibited no discernable T_b change upon control PBS
239 administration (minimal T_b = 33.3 ± 2.4ºC, P = 0.8959 relative to normothermia). In

240 addition, CLZ treatment of Gq-DREADD-expressing animals (n = 6), but not PBS
241 treatment of the same animals (n = 6) or PBS/CLZ treatment of hamsters injected with a
242 control viral construct (n = 3), induced behaviors consonant with torpor entry, including a
243 curled posture and prolonged inactivity in the nest (P = 0.0168, Fig. 5h, i, Extended Data
244 Fig. 12, Supplementary Video 1). Moreover, follow-up analyses revealed that the depth
245 of CLZ-induced torpor across animals correlated with levels of aPOA Gq-DREADD
246 expression, suggesting that more extensive aPOA^{Vglut2} neuron activation drives deeper
247 torpor-like bouts (r = -0.9577, P = 0.0104, Extended Data Fig. 11c, d). Together, these
248 findings show that aPOA^{Vglut2} neuronal activity is both necessary and sufficient to initiate
249 a profound T_b decrease and DT-associated nesting behaviors in the hamster.

250 Finally, given that aPOA^{Vglut2} neurons are present in both the Syrian hamster (a
251 hibernator) and mouse (non-hibernator), we investigated whether virus-mediated
252 chemogenetic activation of this neuronal population in mice housed at low ambient
253 temperatures would drive a DT-like decrease in T_b. Indeed, CLZ treatment of Samd3E-
254 Gq-DREADD-transduced mice yielded a rapid and sustained drop in body temperature,
255 although markedly less than that observed in hamsters (Extended Data Fig. 13). Thus,
256 aPOA^{Vglut2} neuronal activation is sufficient to elicit acute, pronounced reductions in core
257 temperature in both hibernating and non-hibernating species, with the difference in
258 magnitude suggestive of potential hibernator-specific evolutionary modifications in
259 downstream effector circuitry.

260

261 **Discussion**

262 Hibernation is a recurrently evolved survival strategy across the mammalian
263 lineage defined by a regulated multi-day decrease in metabolic rate and body
264 temperature, known as torpor[2,3]. Entry into this state is orchestrated by a complex
265 interplay of environmental cues and internal signals[84]. However, despite decades of work,
266 including reports of hibernation-associated neural activity changes and classic lesion
267 studies implicating the hypothalamus[39,62,64,65], the specific neuronal populations that
268 initiate entry into hibernation-associated torpor have remained undefined. Here, using a
269 Syrian hamster model, we combine neural activity mapping with chemogenetic
270 manipulation to demonstrate that activity within the aPOA is required for entry into deep
271 torpor entry.

272 Our single-nucleus transcriptional and epigenomic profiling of the hamster POA
273 revealed strong cellular homology with the mouse, and surprisingly no evidence of
274 hibernator-specific neuronal cell types. Instead, we observed that *Samd3*-expressing
275 aPOA glutamatergic neurons exhibit elevated activity upon hibernation-associated DT in
276 the hamster. Leveraging our multiomic POA atlas, we developed an enhancer-driven AAV
277 that enables selective access to this population. Using this tool, we show that silencing
278 aPOA^{Vglut2} neurons blocks deep torpor entry, whereas chemogenetic activation of the
279 same population is sufficient to drive a rapid reduction in body temperature accompanied
280 by torpor-associated nesting behavior. Together, these studies establish Samd3E-AAV-
281 targeted aPOA^{Vglut2} neurons as key regulators of hibernation entry and provide the first
282 genetic access to neural circuits controlling this complex physiological state. Moreover,
283 the Samd3E-AAV and the underlying enhancer-driven viral targeting strategy will be
284 broadly applicable for dissecting hibernation circuit elements in other species and

285 examining whether hibernation circuitry is conserved across hibernators, including
286 primates.

287 Although fasting-induced daily torpor and seasonal hibernation both involve
288 reductions in body temperature, metabolic rate, and heart rate, these states differ
289 markedly in their depth, duration, and ethological context. FIT in mice represents a short-
290 term response to food scarcity, lasting only hours[2,3,85–87], whereas hibernation is a
291 seasonal behavior involving deeper, multi-day torpor bouts punctuated by brief periods of
292 interbout euthermia. While the evolutionary origin of these adaptations remains a subject
293 of debate, our findings raise the possibility that differences between daily torpor and
294 hibernation arise from species-specific connectivity or activity patterns within a broadly
295 conserved aPOA^{Vglut2} neuronal population. These differences are potentially shaped by
296 cross-species gene expression differences we observe in these cells (Extended Data Fig.
297 7d). Consistent with this idea, chemogenetic activation of aPOA^{Vglut2} neurons in hamsters
298 elicits substantially deeper torpor-like bouts than in mice. It is notable that
299 chemogenetically-induced torpor approached but did not fully recapitulate the body
300 temperature observed in natural deep torpor. This difference may reflect lower viral
301 transduction/targeting efficiency (Extended Data Fig. 10) or may indicate additional circuit
302 components required for full expression of deep torpor. Future studies will be needed to
303 determine whether this aPOA^{Vglut2} population or the broader hibernation circuitry
304 undergoes active remodeling during the prolonged pre-hibernation conditioning period.

305 More broadly, our findings of a shared circuit node regulating daily torpor and
306 seasonal hibernation provide further support for the idea that regulated heterothermy is
307 an ancestral mammalian trait[88,89]. This would further suggest that core elements of

308 torpor-inducing circuitry are conserved across all mammals, including in species that do
309 not naturally hibernate. Consistent with this notion, *in situ* hybridization data from the
310 marmoset (*Callithrix jacchus*), a non-hibernating primate, indicate that neurons
311 expressing torpor-associated markers are present in homologous regions of the
312 aPOA[90–92] (Extended Data Fig. 14). The Samd3E-AAV that we developed is an ideally
313 suited tool to investigate the degree to which activating these torpor-associated
314 neuronal population in non-hibernators, including non-human primates, could induce a
315 synthetic torpor-like state.

316 Together, we identify a neuronal population that controls hibernation, enabling for
317 the first time the ability to initiate, manipulate and study this fascinating adaptation. Our
318 work establishes a foundation for future efforts to define the broader neural architecture
319 of hibernation, including upstream pathways conveying seasonal and metabolic cues,
320 downstream effectors mediating systemic adaptation, and the cellular mechanisms that
321 permit neurons and other organs to function at near-freezing temperatures. Beyond
322 advancing our understanding of mammalian physiology, these insights may ultimately
323 inform approaches to harness hibernation-related mechanisms for therapeutic
324 hypothermia, organ preservation, metabolic control, protection from muscle atrophy,
325 aging-related decline, and perhaps even space travel.

326 **Methods**

327 **Animals**

328 Animal experiments were approved by the Massachusetts Institute of Technology
329 Committee of Animal Care (Protocol 2503000788), following ethical guidelines described
330 in the US National Institutes of Health Guide for the Care and Use of Laboratory Animals
331 and the Animal Welfare Act.

332 **Hamster.** For all experiments, unless otherwise noted, adult female (5-6-week-
333 old) Syrian hamsters (Inotiv, Strain HsdHan:AURA, Stock 089) were used. Hamsters
334 were singly caged and initially housed at 22°C under a standard 12-hour light/dark cycle
335 (12L:12D) cycle in temperature- and humidity-controlled rooms and had *ad libitum* access
336 to food and water.

337 **Mouse.** Adult female (8-week-old) C57BL/6J (JAX #000664) mice were used. All
338 mice were group housed initially at 22°C under a standard 12L:12D cycle in temperature-
339 and humidity-controlled rooms and had *ad libitum* access to food and water.

340 No statistical methods were used to predetermine the sample size. Hamsters were
341 randomly assigned to experimental groups before surgery. Where possible, investigators
342 were blinded during analysis.

343

344 **Hibernation Induction**

345 Utilizing a modified hibernation paradigm[61,93] female (5-6-week-old) hamsters
346 were singly caged and housed at 22°C under a standard 12L:12D cycle for a short period
347 to acclimate to the animal facility. Upon completion of acclimation, hamsters were
348 transferred to a reduced 8L:16D cycle with an ambient temperature of 22°C. After 7-8

349 weeks, hamsters were placed in temperature-controlled chambers with 8L:16D cycle and
350 ambient temperatures of 4-5°C. Initiation of hibernation was confirmed by changes in T_b
351 measured by telemetric temperature probes. In all cases, hamsters had *ad libitum* access
352 to food and water.
353
354 **Telemetric monitoring of core body temperature**
355 Within the 7-8-week period of housing at 22°C in 8L:16D cycle, hamsters were
356 anesthetized with 3% isoflurane and implanted with telemetric/logger temperature probes
357 (Star-Oddi, DST microRF-T) in the abdominal cavity. Hamsters were allowed to recover
358 for a minimum of three days before additional procedures or experiments were performed.
359 After recovery and at the end of the 7-8-week period, hamsters were moved to
360 temperature-controlled chambers, and core body temperature was monitored in home
361 cages placed onto a radio frequency receiver antenna (Star-Oddi, Antenna & RF-box).
362 Upon euthanasia, probes were removed and complete logged data downloaded. Core
363 body temperature was logged every 20-30 min.
364
365 **Torpor bout analysis**
366 **Classification.** To classify torpor bouts, we employed a Gaussian Mixture Model
367 in R. The classification was based on minimum body temperature and bout duration. Each
368 bout was assigned to the cluster in which it had the highest posterior probability of
369 membership. A cluster characterized by lower T_b and longer duration was designated as
370 "Deep", whereas the other cluster was classified as "Shallow". Furthermore, periods of
371 between bouts above the set T_b threshold were classified as IBE.

372 **Circadian preference.** In R, circadian preference for torpor and IBE initiation was
373 quantified using the Raleigh test of circular uniformity.
374 **Exponential decay.** In R, elapsed time in torpor for each body temperature
375 reading from torpor bouts classified as deep were determined for the first 30 hours. Next,
376 using the mean of temperatures at each time across animals, a nonlinear model was fit
377 to the data using the minimum temperature within the 30-hour period as a fixed asymptotic
378 value.
379

380 **Viral constructs**

381 AAV8-hSyn-hM4D(Gi)-mCherry (Addgene, 50475-AAV8) was obtained from
382 Addgene. AAV8-Samd3E-dTomato-nlsdTomato, AAV8-Samd3E-hM4D(Gi)-P2A-
383 nlsGFP, AAV8-Samd3E-EGFP-P2A-Synaptophysin-mRuby, and AAV8-Samd3E-
384 hM3D(Gq)-P2A-nlsGFP were produced in-house using the method previously
385 described[94] and titered via digital PCR (QIAGEN, QIAcuity). All viruses were diluted with
386 PBS to a final titer of 1E13 vg/mL before stereotaxic delivery into the hamster brain. For
387 mice, AAV8-Samd3E-hM3D(Gq)-P2A-nlsGFP with a final titer of 5E13 vg/mL was used.
388

389 **Stereotaxic viral injection**

390 **Hamster.** Hamsters were anaesthetized with 3% isoflurane and placed in a
391 stereotaxic head frame (David Kopf Instruments, model 1900). If hamsters were actively
392 hibernating, they were aroused from hibernation and placed at 22°C the day prior to
393 surgery. An air-based injection system connected to a pulled glass needle was used to
394 infuse ~100 nL of virus bilaterally at regions of interest. Hypothalamic regions were

395 targeted by referencing the hamster stereotaxic atlas[95]. When targeting the aPOA,
396 coordinates +1.2 mm AP, ±0.4 mm ML, -7.5mm DV were used. Hamsters were allowed
397 to recover at 22°C for a minimum of 3 days before a return to 4°C chambers. Animals
398 were afforded a recovery period of at least two weeks post-surgery prior to further
399 experimental manipulation to allow for viral expression and, if appropriate, resumption of
400 hibernation.

401 **Mouse.** Mice were anesthetized with 3% isoflurane and placed in a stereotaxic
402 head frame (RWD, Guangdong, China). A Nanoject III (Drummond Scientific, Broomall,
403 PA) system connected to a pulled glass needle was used to infuse ~100 nL of virus
404 bilaterally into the aPOA (distance from Bregma, AP: +0.6 mm, ML: ±0.4 mm, DV: -5.2
405 mm). Mice were monitored for three days post-surgery to ensure full recovery, with a
406 waiting period of at least two weeks to allow sufficient viral expression.

407

408 **Chemogenetic manipulations**

409 **Hamster.** Clozapine dihydrochloride (Hello Bio, HB6129) was either dissolved in
410 sterile water or PBS at a concentration of 10 mg/mL and then stored at -20°C until use.
411 For administration via drinking water, CLZ dissolved in sterile water was diluted in drinking
412 water at a dose of 0.1 mL/kg (1 mg/kg) in a final volume of 250 mL. Animals were
413 maintained on CLZ water for 3-7 days. For intraperitoneal (I.P.) administration, CLZ
414 dissolved in PBS was administered at a dose of 0.5 mL/kg (5 mg/kg). In each case when
415 treating actively hibernating hamsters, they were aroused from hibernation the morning
416 of each experiment and treatment was administered in the evening.

417 **Mouse.** Mice injected with AAV8-Samd3E-hM3D(Gq)-P2A-nlsGFP were single
418 housed and placed in a temperature-controlled chamber at 8°C for three days. After three
419 days, mice were I.P. injected with CLZ at a dose of 5 mg/kg and surface body temperature
420 was measured using a thermal camera (Teledyne FLIR C5, Teledyne Flir, Wilsonville,
421 OR). Images were taken before CLZ injection, and 30 min, 60 min, 3 hours, 6 hours and
422 24 hours after CLZ injection. Analysis of surface body temperature and representative
423 images were generated using the Flir Ignite software (https://ignite.flir.com/).
424
425 **Immunofluorescence**
426 Hamsters were deeply anesthetized with isoflurane and then euthanized by
427 transcardial perfusion of 50 mL ice-cold 1X PBS followed by 50 mL of 4%
428 paraformaldehyde (PFA). Brains were extracted, post-fixed overnight with 4% PFA at
429 4°C, and then embedded in 1X PBS with 3% agarose. Brains were sliced on a vibratome
430 into 50 µm coronal sections and stored at -20°C in cryoprotectant buffer (30% sucrose,
431 1% polyvinyl-pyrrolidone (PVP-40), 30% ethylene glycol, in 0.1 M phosphate buffer).
432 Free-floating coronal sections were washed three times with 1X PBS and then blocked
433 for 1 hour at room temperature with 1X PBS containing 10% donkey serum and 0.3%
434 Triton X-100. Sections were incubated overnight at 4°C with primary antibodies (Rabbit
435 anti-FOS, Synaptic Systems, 226-008; Rabbit anti-RFP, Rockland, 600-401-379; Chicken
436 anti-GFP, Aves Labs, GFP-1020) diluted in 1X PBS containing 5% donkey serum and
437 0.3% Triton X-100, washed again three times with 1X PBS, and incubated for 2 hours at
438 room temperature with secondary antibodies in 1X PBS containing 5% donkey serum and
439 0.3% Triton X-100. After washing three times in 1X PBS, samples were counter-stained

440 for 15 minutes at room temperature with 1 µg/mL DAPI, washed again three times in 1X
441 PBS, and then mounted onto SuperFrost Plus glass slides and coverslipped using
442 Fluoromount-G.
443
444 **Determining deep torpor-active brain regions**
445 Brains were collected in torpor, IBE, and from non-hibernating control animals and
446 were processed as indicated in the section 'Immunofluorescence' using the following
447 reagent for the detection of FOS: Rabbit anti-FOS, Synaptic Systems, 226-008.
448 **Sample imaging.** Sections were imaged with a TissueFAXS SL whole-slide
449 scanning system equipped with a Zeiss Axio Imager Z2 fluorescence microscope and
450 TissueFAXS image acquisition software (Ragon Institute Microscopy Core).
451 **Image analysis**. Using TissueQuest analysis software (TissueGnostics GmbH,
452 Vienna, Austria), brain regions were manually annotated and nuclear DAPI signal
453 segmented. Segmented cells containing putative FOS signal were determined to be FOS-
454 positive based on diameter and mean fluorescence intensity. In R, regional cell counts
455 were analyzed and percent active neurons determined by the fraction of FOS-positive
456 and total DAPI-positive cells. Significance was calculated using a mixed-effects ANOVA
457 with post-hoc pairwise comparisons. Pairwise comparison p-values were multiple tests
458 corrected using the Bonferonni method.
459
460 **Mapping of virally injected hypothalamic nuclei and correlation with**
461 **chemogenetically induced torpor perturbation**

462 Hibernating hamsters were bilaterally injected with AAV8-hSyn-hM4D(Gi)-
463 mCherry. Upon resumption of hibernation, hamsters were administered CLZ water for ~3
464 days (74 hours) to inhibit virally injected regions, and their core body temperature were
465 recorded.

466 **Temperature data analysis.** Upon CLZ water treatment, hamsters reinitiating
467 deep torpor within 48 hours were classified as unperturbed, and those failing to reinitiate
468 (remaining euthermic) within this time were classified as perturbed. Sham surgery control
469 animals treated with CLZ water for 7 days informed this threshold (Extended Data Fig.
470 2c). Absolute elapsed time of euthermia from start of treatment was used for further
471 analysis.

472 **Sample imaging.** Given the unavoidable variability in hypothalamic region
473 targeting and viral spread, all hamsters were euthanized for post hoc assessment of
474 transduced brain regions. Collected brains were processed as indicated in the section
475 'Immunofluorescence' to detect endogenous mCherry fluorescence. Sections were
476 imaged with a TissueFAXS SL whole-slide scanning system equipped with a Zeiss Axio
477 Imager Z2 fluorescence microscope and TissueFAXS image acquisition software (Ragon
478 Institute Microscopy Core).

479 **Image and correlation analysis.** Viral mCherry expression was quantified across
480 70 hypothalamic regions in a semi quantitative manner, where the viral expression was
481 scored 0 (none), 1 (minimal), 2 (partial), or 3 (complete) in each region and hemisphere.
482 The analysis was performed blinded to whether perturbation of torpor was observed in
483 each hamster. To assign a single numeric value for each hypothalamic region in each
484 hamster, we added the semiquantitative expression values from each hemisphere. Next,

485 a Pearson correlation was calculated for each region across all hamsters between the
486 viral expression in that region and the length of time spent euthermic.
487
488 **Nuclei dissociation and single-cell analysis**
489 Preoptic area tissue was dissected from adult male and female Syrian hamsters
490 and immediately flash-frozen. The 10X genomics nuclei isolation kit (1000448) was used
491 to obtain dissociated nuclei. Tissue was homogenized on ice in a detergent-based nuclei
492 isolation buffer, passed through a 40-µm filter, and purified by centrifugation. Nuclei were
493 washed, and counted before loading. Single-nucleus multiome libraries were prepared
494 using the 10x Genomics Chromium Single Cell Multiome ATAC + Gene Expression
495 workflow following the manufacturer's protocol. Constructed libraries were quantified,
496 pooled, and sequenced on an Illumina platform to recommended depth for both
497 modalities. The raw data were processed in parallel with cellranger-arc to generate gene-
498 expression count matrices, ATAC fragment files, and peak-by-cell accessibility matrices.
499 A recently published mouse POA multiome dataset generated with the same 10x system
500 was obtained to build a reference dataset. A combination of scVI and Scanpy[96,97]
501 pipelines were used to process and integrate the two datasets, including quality control
502 (filtering by gene counts, UMI counts, and mitochondrial RNA content), normalization, log-
503 transformation, identification of highly variable genes, dimensionality reduction,
504 neighborhood graph construction, and Leiden clustering.
505 To ensure that downstream analyses focused on POA-associated neuronal
506 populations, we used the MERFISH dataset as a spatial reference[76]. To this end, mouse
507 spatial transcriptomic data was subset to only include neurons found in the mPOA and

508 co-clustered with mouse neuronal snRNA-seq. Canonical POA markers and spatial
509 annotations were used to confirm that the identified clusters in both species corresponded
510 to POA-localized neuronal subtypes. Subsequently, the reference mouse dataset was
511 used to identify homologous hamster neurons through integration and label transferring
512 with scANVI[98]. Chromatin accessibility matrices were analyzed with Pycistopic[99] including
513 psuedobulking, peak calling and filtering, identification of co-accessible regions and
514 differential accessibility analysis.
515
516 **Double fluorescent *in situ* hybridization and immunofluorescence**
517 Hamsters were deeply anesthetized with isoflurane and then euthanized by
518 transcardial perfusion of 50 mL ice-cold 1X PBS followed by 50 mL of 4% PFA. Brains
519 were extracted, post-fixed overnight with 4% PFA at 4°C, and then incubated in 1X PBS
520 with 30% sucrose at 4°C until fully infiltrated and sunk to the bottom of the chamber (72-
521 96 hours). Brains were embedded in Optimal Cutting Temperature (O.C.T.) compound,
522 frozen on dry ice, and stored at -80°C until use. Brains were sliced on a cryostat (Leica
523 CM3050 S) into 10-30 µm coronal sections, placed in cryoprotectant buffer, and stored at
524 −20°C until use. Free-floating coronal sections were washed three times with 1X PBS,
525 mounted onto Superfrost Plus slides, and then baked for 45 minutes at 60°C. Subsequent
526 steps followed the standard fluorescent *in situ* hybridization protocol for the RNAscope
527 Fluorescent Multiplex V2 Assay using the following probes: Mau-*Samd3*-C1 (1826261),
528 Mau-*Slc17a6*-C2 (1176381), Mau-*Adcyap1*-O1-C3 (1808861), Mau-*Slc32a1*-C4
529 (1176381).

530 Upon completion of *in situ* hybridization, samples immediately were processed
531 according to the ACD RNAscope Fluorescent Multiplex V2 Assay Combined with
532 Immunofluorescence manual with the following modifications: Slide-mounted sections
533 were washed twice in 1X TBS with 0.005% Tween-20 (TBST), blocked for 1 hour at room
534 temperature with 1X TBS containing 10% donkey serum, and incubated overnight at 4°C
535 with primary antibodies (Rabbit anti-FOS, Synaptic Systems, 226-008; Rabbit anti-RFP,
536 Rockland, 600-401-379; Chicken anti-GFP, Aves Labs, GFP-1020) diluted in 1X TBS
537 containing 5% donkey serum. Slides were washed three times with TBST, incubated for
538 2 hours at room temperature with secondary antibodies in 1X TBS containing 5% donkey
539 serum, washed again three times with TBST, counter-stained for 15 minutes at room
540 temperature with 1 µg/mL DAPI, washed three times with 1X TBS, and finally mounted
541 on coverslips using ProLong Gold.

542 **Sample imaging.** Sections were either imaged with a TissueFAXS SL whole-slide
543 scanning system equipped with a Zeiss Axio Imager Z2 fluorescence microscope and
544 TissueFAXS image acquisition software (Koch Institute Swanson Biotechnology
545 Center/Microscopy Core) or a Leica Stellaris 8 FALCON confocal microscope (Whitehead
546 Institute W.M. Keck Facility for Biological Imaging).

547 **Image analysis**. Using QuPath software[100], colocalization analysis of RNAscope
548 and immunofluorescent signals was performed. After manual annotation of regions of
549 interest, the InstanSeg extension[101] was utilized for cell segmentation, considering each
550 fluorescent signal. Next, segmented cells containing putative RNAscope and
551 immunofluorescent signals were determined to be positive or negative for associated
552 markers based on diameter and mean fluorescence intensity. Subsequent quantification

553 of counts was performed in R, while plotting and statistical analysis was performed in
554 GraphPad Prism software (Boston, MA).
555
556 **Inhibition of aPOA^{Vglut2} neurons**
557 Hibernating hamsters were bilaterally injected with either AAV8-Samd3E-
558 hM4D(Gi)-P2A-nlsGFP or AAV8-Samd3E-EGFP-P2A-Synaptophysin-mRuby. On the
559 day of treatment, hamsters were aroused in the morning, I.P. injected with CLZ and
560 provided with CLZ water in the evening, I.P. injected again 16 hours later, and core body
561 temperature recorded. This regimen accounted for variability in water intake within the
562 first 24 hours of the experiment and maximized inhibition of our targeted population. A
563 CLZ water treatment window of 6 days (144 hours) was used. For PBS control treatment,
564 an identical regimen was followed.
565 **Temperature data analysis.** In GraphPad Prism (Boston, MA), absolute elapsed
566 time of euthermia from start of treatment was used to determine differences within groups.
567 The treatment window duration (144 hours) was applied as an upper bound for statistical
568 analysis. In R, temperature data from each virus group and treatment condition was
569 mapped to circadian time. In GraphPad Prism (Boston, MA), statistical analysis was
570 performed on temperatures in the light and dark cycles within virus groups.
571
572 **Excitation of aPOA^{Vglut2} neurons**
573 Hamsters were bilaterally injected with either AAV8-Samd3E-hM3D(Gq)-P2A-
574 nlsGFP or AAV8-Samd3E-EGFP-P2A-Synaptophysin-mRuby and housed at 4°C to
575 acclimate. On the day of treatment, hamsters were aroused in the morning, I.P. injected

576 with CLZ in the evening, and core body temperature recorded. For PBS control treatment,
577 an identical regimen was followed.

578 **Temperature data analysis.** In R, temperature data was analyzed using the
579 method described in section 'Torpor bout analysis' to determine if the CLZ induced drop
580 in body temperature clustered with either deep or shallow torpor. In GraphPad Prism
581 (Boston, MA), statistical analysis was performed on minimum temperatures across each
582 condition (euthermia, torpor, CLZ, and PBS).

583 **Sample imaging.** Collected brains were processed as indicated in the section
584 'Immunofluorescence' using the following reagent for the detection of AAV8-Samd3E-
585 hM3D(Gq)-P2A-nlsGFP: Chicken anti-GFP, Aves Labs, GFP-1020. Sections were
586 imaged with a TissueFAXS SL whole-slide scanning system equipped with a Zeiss Axio
587 Imager Z2 fluorescence microscope and TissueFAXS image acquisition software (Koch
588 Institute Swanson Biotechnology Center/Microscopy Core).

589 **Image and correlation analysis.** aPOA GFP expression was quantified in a semi
590 quantitative manner where expression was scored 0 (none), 1 (minimal), 2 (partial), or 3
591 (complete) in each hemisphere. The analysis was performed blinded to change in body
592 temperature observed in each hamster. Hemispheric values were summed within
593 animals. In GraphPad Prism (Boston, MA), a Pearson correlation was performed between
594 GFP viral expression and the minimum body temperature.

595

596 **Behavioral analysis**

597 Hamsters housed at 4°C and injected with AAV8-Samd3E-hM3D(Gq)-P2A-
598 nlsGFP or AAV8-Samd3E-EGFP-P2A-Synaptophysin-mRuby were I.P. injected with PBS

599 (0.5 mL/kg) after a one-hour baseline video recording of homecage behavior and an
600 additional hour recording post injection. Following at least a week recovery in 4°C
601 chambers, animals were injected with CLZ (5 mg/kg) and videos were recorded for one
602 hour before and post drug administration in 4°C chambers. Homecage behaviors were
603 manually coded using BORIS software[102]. Behavior was coded 30 min after PBS or CLZ
604 injection over a 10 min window.

605 **References**

606 1. Heller, H. C. & Hammel, H. T. CNS control of body temperature during hibernation. *Comp.*
607 *Biochem. Physiol. A Physiol.* **41**, 349–359 (1972).
608 2. Geiser, F. Metabolic Rate and Body Temperature Reduction During Hibernation and Daily
609 Torpor. *Annu. Rev. Physiol.* **66**, 239–274 (2004).
610 3. Geiser, F. *Ecological Physiology of Daily Torpor and Hibernation*. (Springer, Cham,
611 Switzerland, 2021).
612 4. Drew, K. L. *et al.* Central nervous system regulation of mammalian hibernation: implications
613 for metabolic suppression and ischemia tolerance. *J Neurochem* **102**, 1713–1726 (2007).
614 5. Heller, H. C. Hibernation: neural aspects. *Annu. Rev. Physiol.* **41**, 305–321 (1979).
615 6. Barnes, B. M. Freeze avoidance in a mammal: body temperatures below 0 degree C in an
616 Arctic hibernator. *Science* **244**, 1593–1595 (1989).
617 7. Tan, C. L. & Knight, Z. A. Regulation of Body Temperature by the Nervous System. *Neuron*
618 **98**, 31–48 (2018).
619 8. Morrison, S. F. & Nakamura, K. Central Mechanisms for Thermoregulation. *Annu. Rev.*
620 *Physiol.* **81**, 285–308 (2019).
621 9. Carey, H. V., Andrews, M. T. & Martin, S. L. Mammalian Hibernation: Cellular and
622 Molecular Responses to Depressed Metabolism and Low Temperature. *Physiol. Rev.* **83**,
623 1153–1181 (2003).
624 10. Logan, S. & Storey, K. Regrowth and neuronal protection are key for mammalian
625 hibernation: roles for metabolic suppression. *Neural Regen. Res.* **15**, 2027 (2020).
626 11. Liu, C. *et al.* The future of artificial hibernation medicine: protection of nerves and organs
627 after spinal cord injury. *Neural Regen. Res.* **19**, 22–28 (2024).

628 12. Wu, C. *et al.* Insights of mammalian hibernator-derived cholangiocyte organoids in
629 improving liver cold preservation. *Protein Cell* pwaf052 (2025) doi:10.1093/procel/pwaf052.
630 13. He, W. *et al.* Modeling mammalian hibernation to improve organ cold preservation: Using
631 the intestine as an example. *Cell Res.* **35**, 691–694 (2025).
632 14. Drew, K. L. *et al.* Opportunities and barriers to translating the hibernation phenotype for
633 neurocritical care. *Front. Neurol.* **14**, 1009718 (2023).
634 15. Lyman, C. P. & Fawcett, D. W. The effect of hibernation on the growth of sarcoma in the
635 hamster. *Cancer Res.* **14**, 25–28 (1954).
636 16. Ou, J. *et al.* iPSCs from a Hibernator Provide a Platform for Studying Cold Adaptation and
637 Its Potential Medical Applications. *Cell* **173**, 851-863.e16 (2018).
638 17. Lyman, C. P., O'Brien, R. C., Greene, G. C. & Papafrangos, E. D. Hibernation and
639 Longevity in the Turkish Hamster *Mesocricetus brandti*. *Science* **212**, 668–670 (1981).
640 18. Jayne, L. *et al.* A torpor-like state in mice slows blood epigenetic aging and prolongs
641 healthspan. *Nat. Aging* **5**, 437–449 (2025).
642 19. Al-attar, R. & Storey, K. B. Suspended in time: Molecular responses to hibernation also
643 promote longevity. *Exp. Gerontol.* **134**, 110889 (2020).
644 20. Cerri, M., Hitrec, T., Luppi, M. & Amici, R. Be cool to be far: Exploiting hibernation for
645 space exploration. *Neurosci. Biobehav. Rev.* **128**, 218–232 (2021).
646 21. Tøien, Ø. *et al.* Hibernation in Black Bears: Independence of Metabolic Suppression from
647 Body Temperature. *Science* **331**, 906–909 (2011).
648 22. Dausmann, K. H. & Warnecke, L. Primate Torpor Expression: Ghost of the Climatic Past.
649 *Physiology* **31**, 398–408 (2016).

650 23. Dawe, A. R. & Spurrier, W. A. Hibernation Induced in Ground Squirrels by Blood
651 Transfusion. *Science* **163**, 298–299 (1969).
652 24. Oeltgen, P. R. *et al.* Hibernation "trigger": Opioid-like inhibitory action on brain function of
653 the monkey. *Pharmacol. Biochem. Behav.* **17**, 1271–1274 (1982).
654 25. Horton, N. D. *et al.* Isolation and partial characterization of an opioid-like 88 kDa
655 hibernation-related protein. *Comp. Biochem. Physiol. B Biochem. Mol. Biol.* **119**, 787–805
656 (1998).
657 26. Kondo, N. *et al.* Circannual Control of Hibernation by HP Complex in the Brain. *Cell* **125**,
658 161–172 (2006).
659 27. Teague, R. S. & Ranson, S. W. The role of the anterior hypothalamus in temperature
660 regulation. *Am. J. Physiol.-Leg. Content* **117**, 562–570 (1936).
661 28. Hammel, H. T. & Pierce, J. B. Regulation of Internal Body Temperature. *Annu. Rev. Physiol.*
662 **30**, 641–710 (1968).
663 29. Zaretskaia, M. V., Zaretsky, D. V., Shekhar, A. & DiMicco, J. A. Chemical stimulation of
664 the dorsomedial hypothalamus evokes non-shivering thermogenesis in anesthetized rats.
665 *Brain Res.* **928**, 113–125 (2002).
666 30. Nakamura, K. & Morrison, S. F. A thermosensory pathway that controls body temperature.
667 *Nat Neurosci* **11**, 62–71 (2008).
668 31. Hensel, H. Neural processes in thermoregulation. *Physiol. Rev.* **53**, 948–1017 (1973).
669 32. Jessen, C. Thermal afferents in the control of body temperature. *Pharmacol. Ther.* **28**, 107–
670 134 (1985).
671 33. Hammel, H. T., Hardy, J. D. & Fusco, M. M. Thermoregulatory responses to hypothalamic
672 cooling in unanesthetized dogs. *Am J Physiol* **198**, 481–6 (1960).

673 34. Magoun, H. W., Harrison, F., Brobeck, J. R. & Ranson, S. W. Activation of heat loss
674 mechanisms by local heating of the brain. *J. Neurophysiol.* **1**, 101–114 (1938).
675 35. Tan, C. L. *et al.* Warm-Sensitive Neurons that Control Body Temperature. *Cell* **167**, 47-
676 59.e15 (2016).
677 36. Song, K. *et al.* The TRPM2 channel is a hypothalamic heat sensor that limits fever and can
678 drive hypothermia. *Science* **353**, 1393–1398 (2016).
679 37. Yu, S. *et al.* Glutamatergic Preoptic Area Neurons That Express Leptin Receptors Drive
680 Temperature-Dependent Body Weight Homeostasis. *J Neurosci* **36**, 5034–46 (2016).
681 38. Zhou, Q. *et al.* Hypothalamic warm-sensitive neurons require TRPC4 channel for detecting
682 internal warmth and regulating body temperature in mice. *Neuron* **111**, 387-404 e8 (2023).
683 39. Cheng, M. *et al.* Brainstem catecholaminergic neurons induce torpor during fasting by
684 orchestrating cardiovascular and thermoregulation changes. *Nat. Commun.* **16**, 5954 (2025).
685 40. Hrvatin, S. *et al.* Neurons that regulate mouse torpor. *Nature* **583**, 115–121 (2020).
686 41. Takahashi, T. M. *et al.* A discrete neuronal circuit induces a hibernation-like state in rodents.
687 *Nature* **583**, 109–114 (2020).
688 42. Zhang, Z. *et al.* Estrogen-sensitive medial preoptic area neurons coordinate torpor in mice.
689 *Nat. Commun.* **11**, 6378 (2020).
690 43. Machado, N. L. S. *et al.* Preoptic EP3R neurons constitute a two-way switch for fever and
691 torpor. *Nature* 1–10 (2025) doi:10.1038/s41586-025-09056-1.
692 44. Ambler, M., Hitrec, T., Wilson, A., Cerri, M. & Pickering, A. Neurons in the Dorsomedial
693 Hypothalamus Promote, Prolong, and Deepen Torpor in the Mouse. *J. Neurosci. Off. J. Soc.*
694 *Neurosci.* **42**, 4267–4277 (2022).

695 45. Vitale, P. M., Darrow, J. M., Duncan, M. J., Shustak, C. A. & Goldman, B. D. Effects of
696 photoperiod, pinealectomy and castration on body weight and daily torpor in Djungarian
697 hamsters (Phodopus sungorus). *J. Endocrinol.* **106**, 367–375 (1985).
698 46. Paul, M. J., Kauffman, A. S. & Zucker, I. Feeding schedule controls circadian timing of daily
699 torpor in SCN-ablated Siberian hamsters. *J. Biol. Rhythms* **19**, 226–237 (2004).
700 47. Magariños, A. M., McEwen, B. S., Saboureau, M. & Pevet, P. Rapid and reversible changes
701 in intrahippocampal connectivity during the course of hibernation in European hamsters.
702 *Proc. Natl. Acad. Sci. U. S. A.* **103**, 18775–18780 (2006).
703 48. Korhonen, T., Mustonen, A.-M., Nieminen, P. & Saarela, S. Effects of cold exposure,
704 exogenous melatonin and short-day treatment on the weight-regulation and body temperature
705 of the Siberian hamster (Phodopus sungorus). *Regul. Pept.* **149**, 60–66 (2008).
706 49. Stanton, T. L., Daley, J. C. & Salzman, S. K. Prolongation of hibernation bout duration by
707 continuous intracerebroventricular infusion of melatonin in hibernating ground squirrels.
708 *Brain Res.* **413**, 350–355 (1987).
709 50. Chmura, H. E. *et al.* Hypothalamic remodeling of thyroid hormone signaling during
710 hibernation in the arctic ground squirrel. *Commun. Biol.* **5**, 492 (2022).
711 51. Tamura, Y., Shintani, M., Nakamura, A., Monden, M. & Shiomi, H. Phase-specific central
712 regulatory systems of hibernation in Syrian hamsters. *Brain Res.* **1045**, 88–96 (2005).
713 52. Olson, J. M. *et al.* Circannual rhythm in body temperature, torpor, and sensitivity to A_1
714 adenosine receptor agonist in arctic ground squirrels. *J. Biol. Rhythms* **28**, 201–207 (2013).
715 53. Jinka, T. R., Tøien, Ø. & Drew, K. L. Season primes the brain in an arctic hibernator to
716 facilitate entrance into torpor mediated by adenosine A(1) receptors. *J. Neurosci. Off. J. Soc.*
717 *Neurosci.* **31**, 10752–10758 (2011).

718 54. Frare, C., Jenkins, M. E., Soldin, S. J. & Drew, K. L. The Raphe Pallidus and the
719 Hypothalamic-Pituitary-Thyroid Axis Gate Seasonal Changes in Thermoregulation in the
720 Hibernating Arctic Ground Squirrel (Urocitellus parryii). *Front. Physiol.* **9**, 1747 (2018).
721 55. Stanton, T. L., Winokur, A. & Beckman, A. L. Seasonal variation in thyrotropin-releasing
722 hormone (TRH) content of different brain regions and the pineal in the mammalian
723 hibernator, Citellus lateralis. *Regul. Pept.* **3**, 135–144 (1982).
724 56. Mohr, S. M. *et al.* Hypothalamic hormone deficiency enables physiological anorexia in
725 ground squirrels during hibernation. *Nat. Commun.* **15**, 5803 (2024).
726 57. Harris, M. B. & Milsom, W. K. Parasympathetic influence on heart rate in euthermic and
727 hibernating ground squirrels. *J. Exp. Biol.* **198**, 931–937 (1995).
728 58. Heldmaier, G., Ortmann, S. & Elvert, R. Natural hypometabolism during hibernation and
729 daily torpor in mammals. *Respir. Physiol. Neurobiol.* **141**, 317–329 (2004).
730 59. Revel, F. G. *et al.* The circadian clock stops ticking during deep hibernation in the European
731 hamster. *Proc. Natl. Acad. Sci.* **104**, 13816–13820 (2007).
732 60. Mohr, S. M., Bagriantsev, S. N. & Gracheva, E. O. Cellular, Molecular, and Physiological
733 Adaptations of Hibernation: The Solution to Environmental Challenges. *Annu. Rev. Cell*
734 *Dev. Biol.* **36**, 315–338 (2020).
735 61. Chayama, Y., Ando, L., Tamura, Y., Miura, M. & Yamaguchi, Y. Decreases in body
736 temperature and body mass constitute pre-hibernation remodelling in the Syrian golden
737 hamster, a facultative mammalian hibernator. *R. Soc. Open Sci.* **3**, 160002 (2016).
738 62. Markussen, F. A. F., Cazarez-Marquez, F., Melum, V. J., Hazlerigg, D. G. & Wood, S. H. c-
739 fos induction in the choroid plexus, tanycytes and pars tuberalis is an early indicator of
740 spontaneous arousal from torpor in a deep hibernator. *J Exp Biol* **227**, (2024).

741 63. Enoki, R. *et al.* Cold-induced suspension and resetting of Ca2+ and transcriptional rhythms
742 in the suprachiasmatic nucleus neurons. *iScience* **26**, 108390 (2023).
743 64. Bratincsak, A. *et al.* Spatial and temporal activation of brain regions in hibernation: c-fos
744 expression during the hibernation bout in thirteen-lined ground squirrel. *J Comp Neurol* **505**,
745 443–58 (2007).
746 65. Weidler, D. J., Earle, A. M., Myers, G. G. & Sieck, G. C. Effect of hypothalamic lesions on
747 temperature regulation in hibernating ground squirrels. *Brain Res.* **65**, 175–179 (1974).
748 66. Hastings, M. H., Maywood, E. S. & Brancaccio, M. Generation of circadian rhythms in the
749 suprachiasmatic nucleus. *Nat. Rev. Neurosci.* **19**, 453–469 (2018).
750 67. Welsh, D. K., Takahashi, J. S. & Kay, S. A. Suprachiasmatic Nucleus: Cell Autonomy and
751 Network Properties. *Annu. Rev. Physiol.* **72**, 551–577 (2010).
752 68. Weaver, D. R. The Suprachiasmatic Nucleus: A 25-Year Retrospective. *J. Biol. Rhythms* **13**,
753 100–112 (1998).
754 69. Andermann, M. L. & Lowell, B. B. Toward a Wiring Diagram Understanding of Appetite
755 Control. *Neuron* **95**, 757–778 (2017).
756 70. Cone, R. D. *et al.* The arcuate nucleus as a conduit for diverse signals relevant to energy
757 homeostasis. *Int. J. Obes.* **25**, S63–S67 (2001).
758 71. Jais, A. & Brüning, J. C. Arcuate Nucleus-Dependent Regulation of Metabolism—Pathways
759 to Obesity and Diabetes Mellitus. *Endocr. Rev.* **43**, 314–328 (2022).
760 72. Van der Werf, Y. D., Witter, M. P. & Groenewegen, H. J. The intralaminar and midline
761 nuclei of the thalamus. Anatomical and functional evidence for participation in processes of
762 arousal and awareness. *Brain Res. Rev.* **39**, 107–140 (2002).
763 73. Jones, B. E. Arousal systems. *Front. Biosci. J. Virtual Libr.* **8**, s438-451 (2003).

764 74. Roth, B. L. DREADDs for Neuroscientists. *Neuron* **89**, 683–694 (2016).
765 75. Kaplan, H. S. *et al.* Sensory input, sex and function shape hypothalamic cell type
766 development. *Nature* https://doi.org/10.1038/s41586-025-08603-0 (2025)
767 doi:10.1038/s41586-025-08603-0.
768 76. Zhang, M. *et al.* Molecularly defined and spatially resolved cell atlas of the whole mouse
769 brain. *Nature* **624**, 343–354 (2023).
770 77. Dimidschstein, J. *et al.* A viral strategy for targeting and manipulating interneurons across
771 vertebrate species. *Nat. Neurosci.* **19**, 1743–1749 (2016).
772 78. Cronin, T. *et al.* Efficient transduction and optogenetic stimulation of retinal bipolar cells by
773 a synthetic adeno-associated virus capsid and promoter. *EMBO Mol. Med.* **6**, 1175–1190
774 (2014).
775 79. Ben-Simon, Y. *et al.* A suite of enhancer AAVs and transgenic mouse lines for genetic
776 access to cortical cell types. *Cell* **188**, 3045-3064 e23 (2025).
777 80. Graybuck, L. T. *et al.* Enhancer viruses for combinatorial cell-subclass-specific labeling.
778 *Neuron* **109**, 1449-1464.e13 (2021).
779 81. Hrvatin, S. *et al.* A scalable platform for the development of cell-type-specific viral drivers.
780 *eLife* **8**, e48089 (2019).
781 82. Nagy, M. A. *et al.* Cis-regulatory elements driving motor neuron-selective viral payload
782 expression within the mammalian spinal cord. *Proc. Natl. Acad. Sci.* **121**, e2418024121
783 (2024).
784 83. Hunker, A. C. *et al.* Enhancer AAV toolbox for accessing and perturbing striatal cell types
785 and circuits. *Neuron* **113**, 1507-1524 e17 (2025).

786 84. Junkins, M. S., Bagriantsev, S. N. & Gracheva, E. O. Towards understanding the neural
787 origins of hibernation. *J. Exp. Biol.* **225**, jeb229542 (2022).
788 85. Sunagawa, G. A. & Takahashi, M. Hypometabolism during Daily Torpor in Mice is
789 Dominated by Reduction in the Sensitivity of the Thermoregulatory System. *Sci. Rep.* **6**, 1–
790 14 (2016).
791 86. Morton, S. R. Torpor and Nest-Sharing in Free-Living Sminthopsis crassicaudata
792 (Marsupialia) and Mus musculus (Rodentia). *J. Mammal.* **59**, 569–575 (1978).
793 87. Swoap, S. J. & Gutilla, M. J. Cardiovascular changes during daily torpor in the laboratory
794 mouse. *Am. J. Physiol.-Regul. Integr. Comp. Physiol.* **297**, R769–R774 (2009).
795 88. Lovegrove, B. G. A phenology of the evolution of endothermy in birds and mammals. *Biol*
796 *Rev Camb Philos Soc* **92**, 1213–1240 (2017).
797 89. Geiser, F., Stawski, C., Wacker, C. B. & Nowack, J. Phoenix from the Ashes: Fire, Torpor,
798 and the Evolution of Mammalian Endothermy. *Front Physiol* **8**, 842 (2017).
799 90. Kita, Y. *et al.* Cellular-resolution gene expression profiling in the neonatal marmoset brain
800 reveals dynamic species- and region-specific differences. *Proc. Natl. Acad. Sci.* **118**,
801 e2020125118 (2021).
802 91. Shimogori, T. *et al.* Digital gene atlas of neonate common marmoset brain. *Neurosci. Res.*
803 **128**, 1–13 (2018).
804 92. Gene Structural Search | Marmoset Gene Atlas. https://gene-atlas.brainminds.jp/gene-
805 structural/.
806 93. Trefna, M. *et al.* The influence of sex and diet on the characteristics of hibernation in Syrian
807 hamsters. *J. Comp. Physiol. [B]* **187**, 725–734 (2017).

808 94. Negrini, M., Wang, G., Heuer, A., Björklund, T. & Davidsson, M. AAV Production
809 Everywhere: A Simple, Fast, and Reliable Protocol for In-house AAV Vector Production
810 Based on Chloroform Extraction. *Curr. Protoc. Neurosci.* **93**, e103 (2020).
811 95. Wood, R. I. & Morin, L. P. *A Stereotaxic Atlas of the Golden Hamster Brain*. (Elsevier
812 Science, 2001).
813 96. Lopez, R., Regier, J., Cole, M. B., Jordan, M. I. & Yosef, N. Deep generative modeling for
814 single-cell transcriptomics. *Nat. Methods* **15**, 1053–1058 (2018).
815 97. Wolf, F. A., Angerer, P. & Theis, F. J. SCANPY: large-scale single-cell gene expression
816 data analysis. *Genome Biol.* **19**, 15 (2018).
817 98. Xu, C. *et al.* Probabilistic harmonization and annotation of single-cell transcriptomics data
818 with deep generative models. *Mol. Syst. Biol.* **17**, e9620 (2021).
819 99. Bravo González-Blas, C. *et al.* cisTopic: cis-regulatory topic modeling on single-cell ATAC-
820 seq data. *Nat. Methods* **16**, 397–400 (2019).
821 100. Bankhead, P. *et al.* QuPath: Open source software for digital pathology image analysis.
822 *Sci. Rep.* **7**, 16878 (2017).
823 101. Goldsborough, T. *et al.* A novel channel invariant architecture for the segmentation of
824 cells and nuclei in multiplexed images using InstanSeg. 2024.09.04.611150 Preprint at
825 https://doi.org/10.1101/2024.09.04.611150 (2024).
826 102. Friard, O. & Gamba, M. BORIS: a free, versatile open-source event-logging software for
827 video/audio coding and live observations. *Methods Ecol. Evol.* **7**, 1325–1330 (2016).
828 103. Lein, E. S. *et al.* Genome-wide atlas of gene expression in the adult mouse brain. *Nature*
829 **445**, 168–176 (2007).
830

831 **Acknowledgments:** We thank M. Alkire, M.M. Chen, J.A. Cheng, and N.T. Nigrin for their
832 assistance with mouse experiments. We also thank additional Hrvatin lab members for
833 their thoughtful input on this project and manuscript. The snRNA-seq and snATAC-seq
834 were performed with the Whitehead Institute Genome Technology Core. Imaging was
835 performed either at the Ragon Institute Microscopy Core, Koch Institute Swanson
836 Biotechnology Center/Microscopy Core, or the Whitehead Institute W.M. Keck Facility for
837 Biological Imaging. This work was supported by the Mathers Foundation Grant, Searle
838 Scholars Program, Pew Charitable Trust, Longevity Impetus Grant from Norn Group,
839 Hevolution Foundation and Rosenkranz Foundation, MIT Research Support Committee
840 Grant, and Howard Hughes Medical Institute Hrabowski Scholar Program.
841 **Author Contributions:** A.J.M. and S.H. conceptualized the study and designed
842 experiments. A.J.M, C.M.R, A.J.L.P, W.L., A.S.L. performed and analyzed experiments.
843 E.C.G. and S.H. advised on the study and obtained funding for the research. A.J.M.,
844 E.C.G., and S.H. wrote the manuscript.
845 **Competing Interests:** Authors declare that they have no competing interests.
846 **Data and materials availability:** Data will be made available on GEO. All other data
847 needed to evaluate the conclusions are available in the main text, the extended data,
848 supplementary materials, and available upon request.

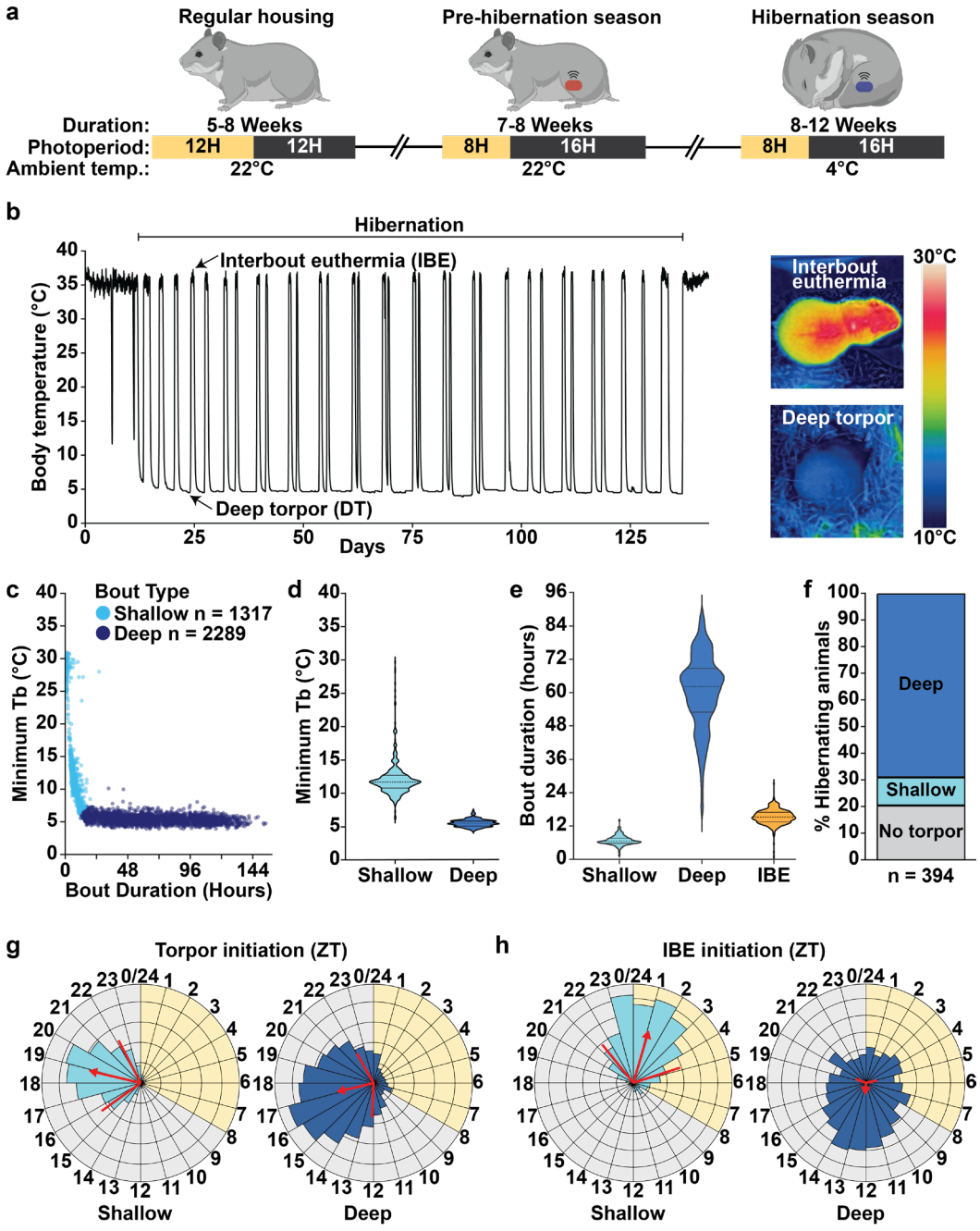

Fig. 1: A laboratory model of Syrian hamster hibernation.

a, A reproducible laboratory model that induces hibernation with stereotyped deep bouts of torpor in Syrian hamsters.

854 **b**, Left: Representative body temperature trace of a hibernating hamster, consisting of
855 repeated bouts of deep torpor (DT) and interbout euthermia (IBE). Right: Thermal images
856 of a hibernating hamster during euthermic and deep torpor intervals.
857 **c**, Classification of torpor bouts as shallow or deep based on minimum temperature and
858 bout duration.
859 **d**,**e**, Violin plots of minimum body temperature (**d**), and duration (**e**) of shallow and deep
860 torpor bouts as well as IBE periods (n = 2471).
861 **f**, Percentage of animals undergoing DT, only shallow torpor, or no torpor bouts within 6
862 weeks of initiating the hibernation period.
863 **g**, Circadian representation (Raleigh plot) of the time of entry into shallow (light blue) or
864 deep (dark blue) torpor bouts. Light and dark cycle phases are represented by yellow and
865 grey, respectively. Red arrow direction and length indicate mean time of initiation and
866 concentration around the mean, respectively. Red lines flanking the arrow indicate s.d.
867 **h**, Circadian representation as in (**g**) of entry into IBE following deep (left, n = 1496) or
868 shallow (right, n = 1011) torpor bouts.

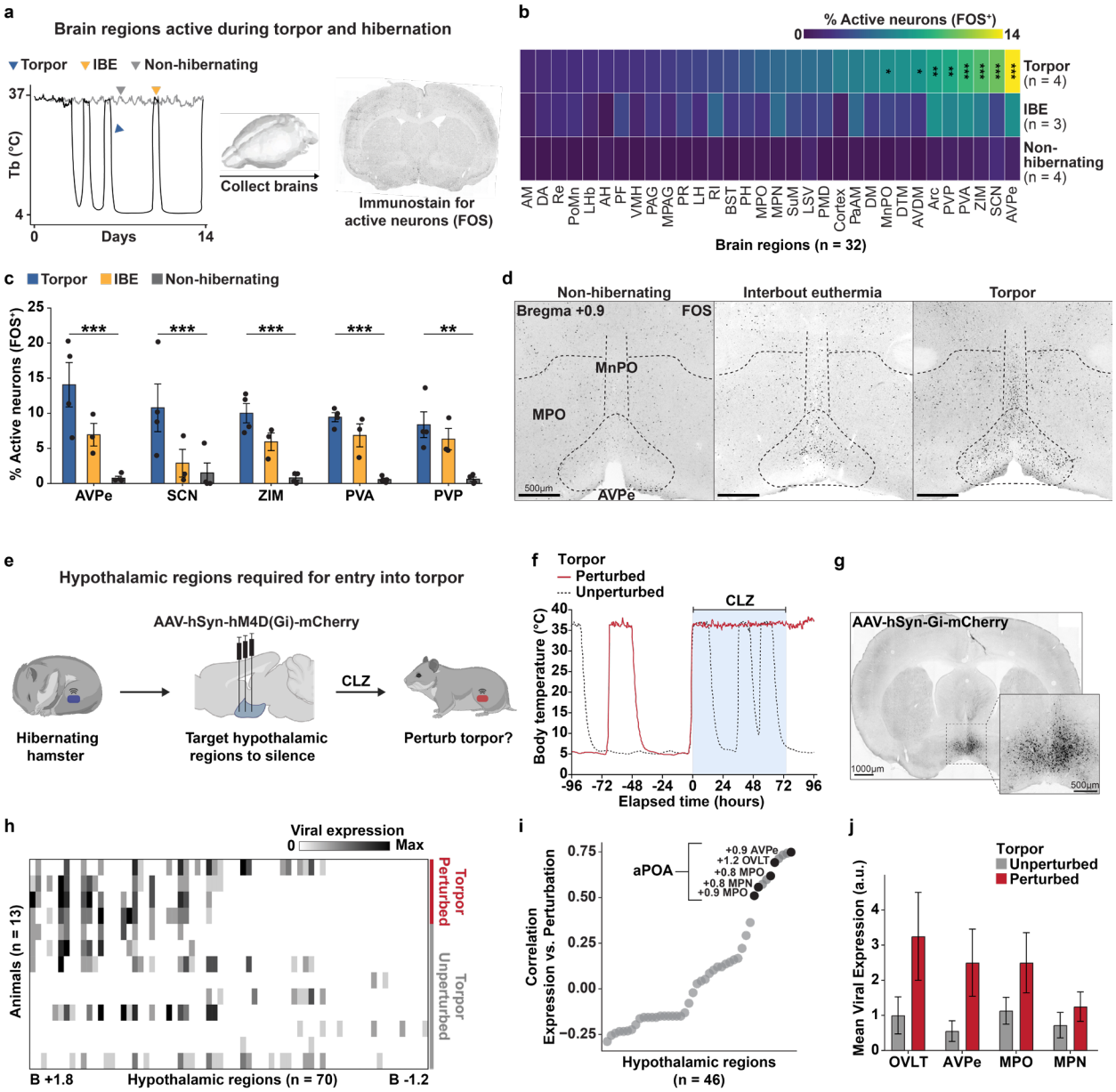

Fig. 2: Identification of anterior preoptic area activity as necessary for deep torpor entry.

a, Strategy for identifying brain regions with hibernation state-dependent activity. Arrows indicate relative sample collection points for torpor, IBE, and non-hibernating animals.

874 **b**,**c**, Hypothalamic and thalamic regions demonstrating an increase in FOS-positive cells
875 in torpor as compared to both IBE and non-hibernating controls (*P-adjusted < 0.05, **P-
876 adjusted < 0.01, ***P-adjusted < 0.001).
877 **d**, FOS immunostaining in the hamster POA across hibernation states. AVPe, MPO, and
878 MnPO denoted by dashed lines.
879 **e**, Strategy for identifying hypothalamic subregions regulating deep torpor entry.
880 **f**, T_b traces showing CLZ-mediated disruption of DT in one Gi-DREADD-mCherry-
881 transduced hamster (solid red) but not the other (dashed black).
882 **g**, Coronal section and inset showing Gi-mCherry expression in the hypothalamus.
883 **h**, Quantification of regional viral Gi-mCherry expression across injected animals.
884 Hypothalamic regions (n = 70) plotted relative to bregma anterior-posterior coordinates.
885 **i**, Correlation of regional viral expression across animals identifies the anterior POA
886 (aPOA) as the region whose inhibition most strongly disrupts DT re-entry.
887 **j**, Higher viral Gi-mCherry expression in aPOA regions from animals exhibiting CLZ-
888 dependent torpor disruption (n = 4) compared to unaffected animals (n = 13). Mean ±
889 s.e.m.

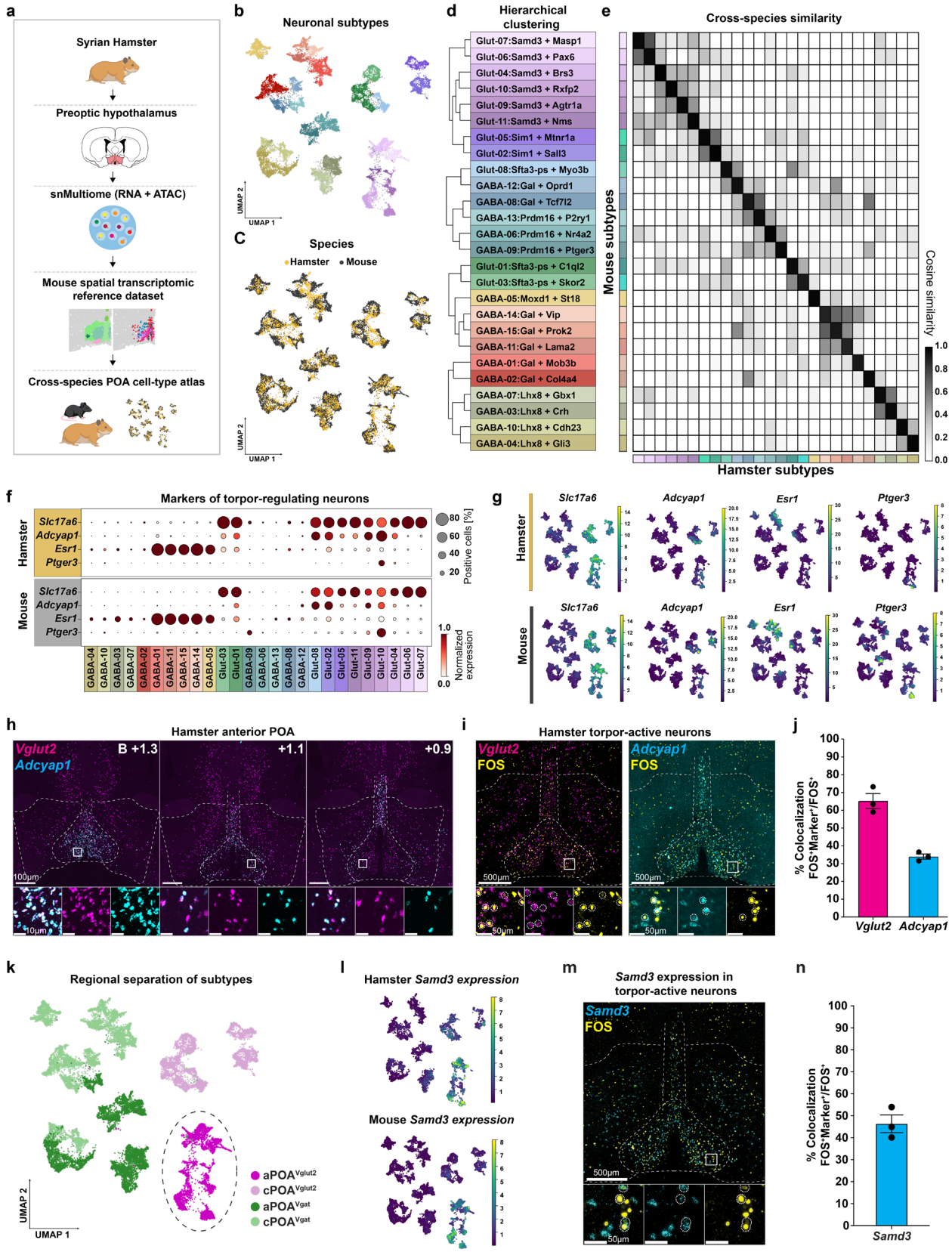
a
Syrian Hamster
Preoptic hypothalamus
snMultiome (RNA + ATAC)
Mouse spatial transcriptomic reference dataset
Cross-species POA cell-type atlas
b
Neuronal subtypes
UMAP 2
UMAP 1
c
Species
Hamster
Mouse
d
Hierarchical clustering
Glut-07:Samd3 + Masp1
Glut-06:Samd3 + Pax6
Glut-04:Samd3 + Brs3
Glut-10:Samd3 + Rxfp2
Glut-09:Samd3 + Agtr1a
Glut-11:Samd3 + Nms
Glut-05:Sim1 + Mtnr1a
Glut-02:Sim1 + Sall3
Glut-08:Sfta3-ps + Myo3b
GABA-12:Gal + Oprd1
GABA-08:Gal + Tcf7l2
GABA-13:Prdm16 + P2ry1
GABA-06:Prdm16 + Nr4a2
GABA-09:Prdm16 + Ptger3
Glut-01:Sfta3-ps + C1ql2
Glut-03:Sfta3-ps + Skor2
GABA-05:Moxd1 + St18
GABA-14:Gal + Vip
GABA-15:Gal + Prok2
GABA-11:Gal + Lama2
GABA-01:Gal + Mob3b
GABA-02:Gal + Col4a4
GABA-07:Lhx8 + Gbx1
GABA-03:Lhx8 + Crh
GABA-10:Lhx8 + Cdh23
GABA-04:Lhx8 + Gli3
e
Cross-species similarity
Mouse subtypes
Hamster subtypes
Cosine similarity
1.0
0.8
0.6
0.4
0.2
0.0
f
Markers of torpor-regulating neurons
Hamster
Mouse
Slc17a6
Adcyap1
Esr1
Ptger3
Positive cells [%]
80
60
40
20
Normalized expression
1.0
0.0
GABA-04
GABA-10
GABA-03
GABA-07
GABA-02
GABA-01
GABA-11
GABA-15
GABA-14
GABA-05
Glut-03
Glut-01
GABA-09
GABA-06
GABA-13
GABA-08
GABA-12
Glut-08
Glut-02
Glut-05
Glut-11
Glut-09
Glut-10
Glut-04
Glut-06
Glut-07
g
Slc17a6
Adcyap1
Esr1
Ptger3
Hamster
Mouse
h
Hamster anterior POA
Vglut2
Adcyap1
B +1.3
+1.1
+0.9
100µm
10µm
i
Hamster torpor-active neurons
Vglut2
FOS
Adcyap1
FOS
500µm
50µm
j
% Colocalization FOS+Marker+/FOS+
100
90
80
70
60
50
40
30
20
10
0
Vglut2
Adcyap1
k
Regional separation of subtypes
UMAP 2
UMAP 1
aPOA^Vglut2
cPOA^Vglut2
aPOA^Vgat
cPOA^Vgat
l
Hamster Samd3 expression
Mouse Samd3 expression
m
Samd3 expression in torpor-active neurons
Samd3
FOS
500µm
50µm
n
% Colocalization FOS+Marker+/FOS+
100
90
80
70
60
50
40
30
20
10
0
Samd3

890

891 **Fig. 3: Cross-species multi-omic mapping identifies a glutamatergic aPOA**
892 **neuronal population active during deep torpor.**

893 **a**, Workflow to generate a cross-species POA cellular taxonomy.

894 **b**,**c**, Uniform manifold approximation and projection (UMAP) plot showing 18,406 nuclei
895 from mice (n = 11) and 8,355 nuclei from Syrian Hamsters (n = 7), indicating 15
896 GABAergic and 11 glutamatergic neuronal subtypes (**b**) or species of origin (**c**).

897 **d**, Hierarchical clustering of the neuronal subtypes.

898 **e**, Cosine similarity analysis showing pairwise transcriptional relatedness between
899 hamster and mouse neuronal subtypes based on mean gene expression.

900 **f**, Dot plot showing FIT-associated marker gene expression across mouse and hamster
901 neuronal subtypes.

902 **g**, UMAP feature plots depicting marker gene expression in the indicated species.

903 **h**, ISH for select FIT-associated marker genes in hamster aPOA.

904 **i**,**j**, Combined FOS immunostaining and ISH analysis for *Slc17a6* (*Vglut2*) and *Adcyap1*
905 from aPOA of hamsters (n = 3) in DT, with accompanying quantification. Mean ± s.e.m.

906 **k**, UMAP plot annotating hamster and mouse POA neurons by regional location based
907 on mouse MERFISH data.

908 **l**, UMAP feature plots depicting *Samd3* expression in the indicated species.

909 **m**,**n**, Combined FOS immunostaining and *Samd3* ISH analysis of aPOA from hamsters
910 (n = 3) in DT, with accompanying quantification. Mean ± s.e.m.

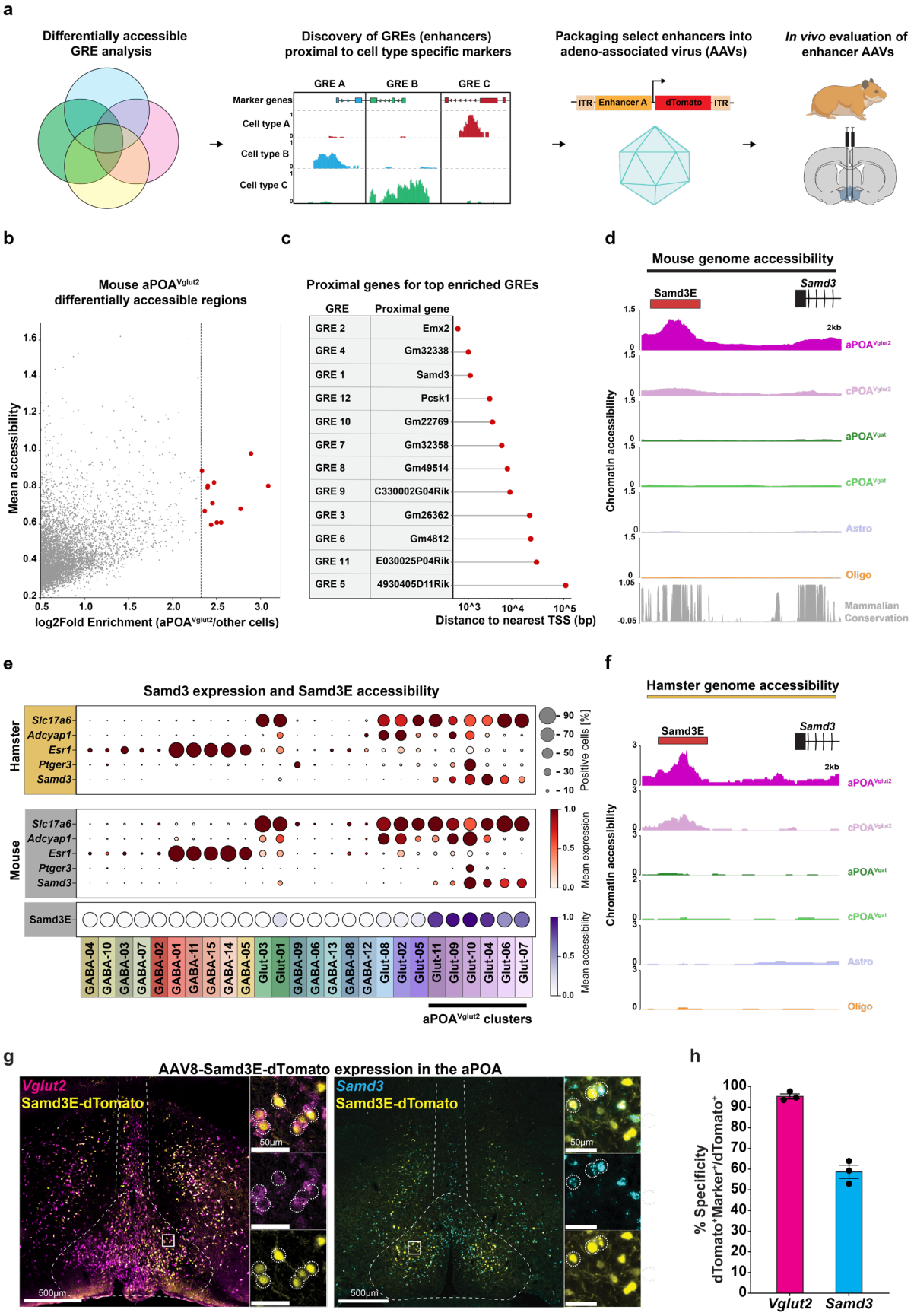
a
Differentially accessible GRE analysis
Discovery of GREs (enhancers) proximal to cell type specific markers
GRE A
GRE B
GRE C
Marker genes
Cell type A
Cell type B
Cell type C
Packaging select enhancers into adeno-associated virus (AAVs)
ITR
Enhancer A
dTomato
ITR
In vivo evaluation of enhancer AAVs
b
Mouse aPOAVglut2 differentially accessible regions
Mean accessibility
log2Fold Enrichment (aPOAVglut2/other cells)
c
Proximal genes for top enriched GREs
GRE
Proximal gene
GRE 2 Emx2
GRE 4 Gm32338
GRE 1 Samd3
GRE 12 Pcsk1
GRE 10 Gm22769
GRE 7 Gm32358
GRE 8 Gm49514
GRE 9 C330002G04Rik
GRE 3 Gm26362
GRE 6 Gm4812
GRE 11 E030025P04Rik
GRE 5 4930405D11Rik
Distance to nearest TSS (bp)
d
Mouse genome accessibility
Samd3E
Samd3
2kb
aPOAVglut2
cPOAVglut2
aPOAVgat
cPOAVgat
Astro
Oligo
Mammalian Conservation
Chromatin accessibility
e
Samd3 expression and Samd3E accessibility
Hamster
Mouse
Slc17a6
Adcyap1
Esr1
Ptger3
Samd3
Samd3E
Positive cells [%]
Mean expression
Mean accessibility
GABA-04 GABA-10 GABA-03 GABA-07 GABA-02 GABA-01 GABA-11 GABA-15 GABA-14 GABA-05 Glut-03 Glut-01 GABA-09 GABA-06 GABA-13 GABA-08 GABA-12 Glut-08 Glut-02 Glut-05 Glut-11 Glut-09 Glut-10 Glut-04 Glut-06 Glut-07
aPOAVglut2 clusters
f
Hamster genome accessibility
Samd3E
Samd3
2kb
aPOAVglut2
cPOAVglut2
aPOAVgat
cPOAVgat
Astro
Oligo
Chromatin accessibility
g
AAV8-Samd3E-dTomato expression in the aPOA
Vglut2
Samd3E-dTomato
Samd3
Samd3E-dTomato
50µm
500µm
h
% Specificity
dTomato+Marker+/dTomato+
Vglut2
Samd3

911

912 **Fig. 4: An enhancer AAV enabling selective targeting of aPOA^{Vglut2} neurons in**
913 **hamsters.**

914 **a**, Workflow for generation of aPOA^{Vglut2} neuron-selective enhancer-AAVs.

915 **b**, Scatter plot of genomic elements (n = 15,208) based on differential accessibility in
916 aPOA^{Vglut2} neurons and mean aPOA^{Vglut2} accessibility signal. Top 10 most differentially
917 accessible elements (FDR-corrected $q < 10^{-300}$) highlighted in red.

918 **c**, Distance to proximal gene transcription start site for the top 10 putative GREs from (**b**).

919 **d**, ATAC-seq genome browser tracks (normalized counts per location) for the mouse
920 *Samd3*-proximal putative GRE (*Samd3E,* red box) in the indicated cell populations in
921 mouse, with accompanying sequence conservation below.

922 **e**, Dotplot depicting *Samd3* gene expression across mouse and hamster POA neuronal
923 subtypes, along with *Samd3E* accessibility in the mouse.

924 **f**, ATAC-seq genome browser tracks (normalized counts per location) for the hamster
925 *Samd3*-proximal putative GRE (*Samd3E*, red box) in the indicated cell populations in
926 hamster.

927 **g**,**h**, Combined immunostaining for viral dTomato and ISH analysis for *Slc17a6* (*Vglut2*)
928 and *Samd3* from aPOA of hamsters injected with AAV8-Samd3E-dTomato, with
929 accompanying quantification. Mean ± s.e.m. (n = 3 animals).

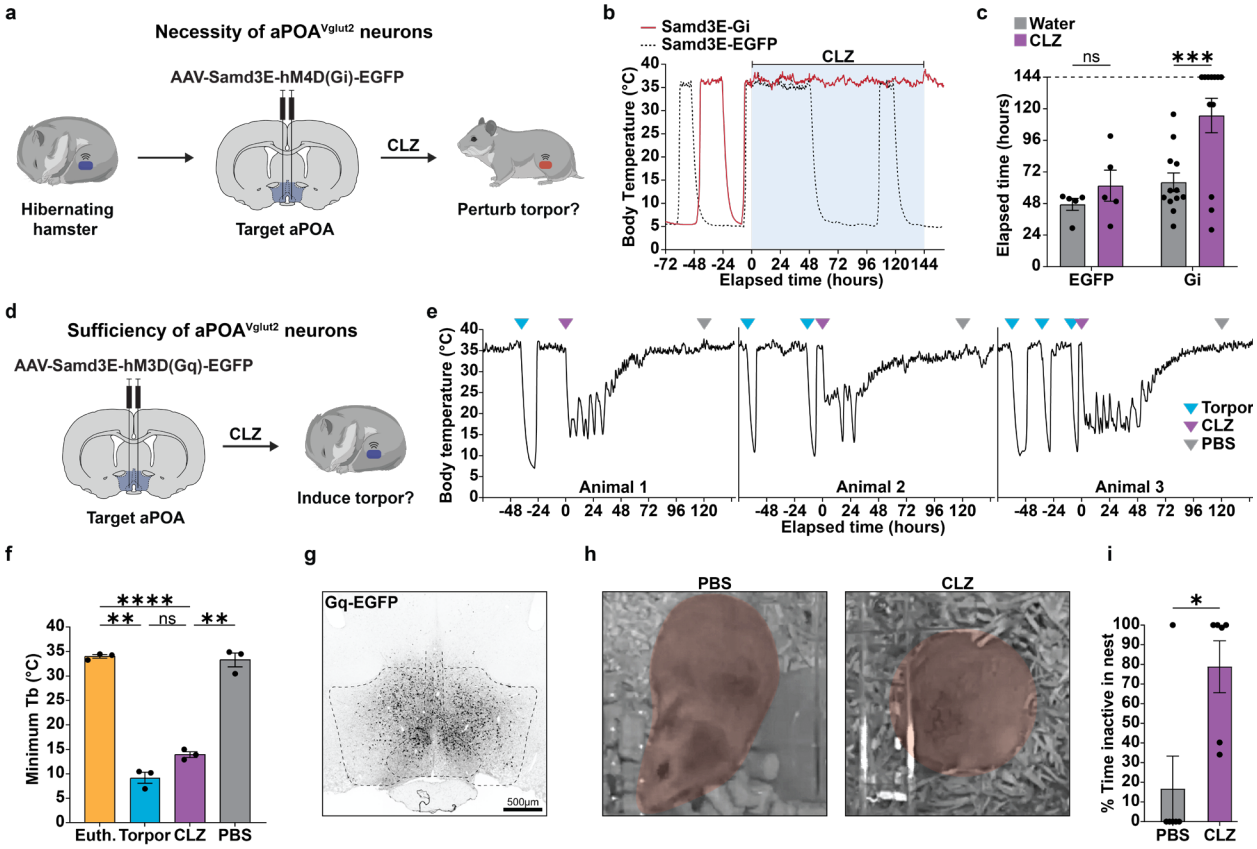

Fig. 5: aPOA glutamatergic neuron activity is necessary and sufficient to induce deep torpor-like entry in hamsters.

a, Strategy for testing the necessity of aPOA^{Vglut2} neuronal activity for DT reentry.

b, T_b traces demonstrating perturbation of torpor resumption upon CLZ administration in Samd3E-Gi-DREADD- but not control Samd3E-EGFP-transduced hamsters.

c, Samd3E-Gi-DREADD-transduced hamsters (n = 12), but not control Samd3E-EGFP-transduced animals (n = 5), show significant perturbations in torpor initiation when administered with CLZ but not water (Šídák's multiple comparisons test).

d, Strategy for testing the sufficiency of aPOA^{Vglut2} neuronal activity for DT entry.

e, T_b traces from Samd3E-Gq-DREADD-injected animals illustrating natural torpor bouts as well as artificial bouts elicited by CLZ administration.

942 **f**, Quantification of minimum T_b reached in Samd3E-Gq-DREADD-transduced animals
943 during euthermic periods, natural deep torpor, and following administration of CLZ or
944 control PBS (n = 3, Tukey's multiple comparisons test).
945 **g**, Coronal section showing Samd3E-Gq-DREADD-EGFP expression in the hamster
946 aPOA.
947 **h**, Images of a Samd3E-Gq-DREADD-transduced hamster following PBS or CLZ
948 treatment.
949 **i**, Percentage of time Samd3E-Gq-DREADD-transduced animals (n = 6) spent inactive in
950 the nest over a 10 min observation window CLZ or control PBS administration (paired t-
951 test).
952 ****P-adjusted < 0.0001, ***P-adjusted < 0.001, **P-adjusted < 0.01, *P-adjusted < 0.05,
953 ns = not significant).

954 **Extended Data**

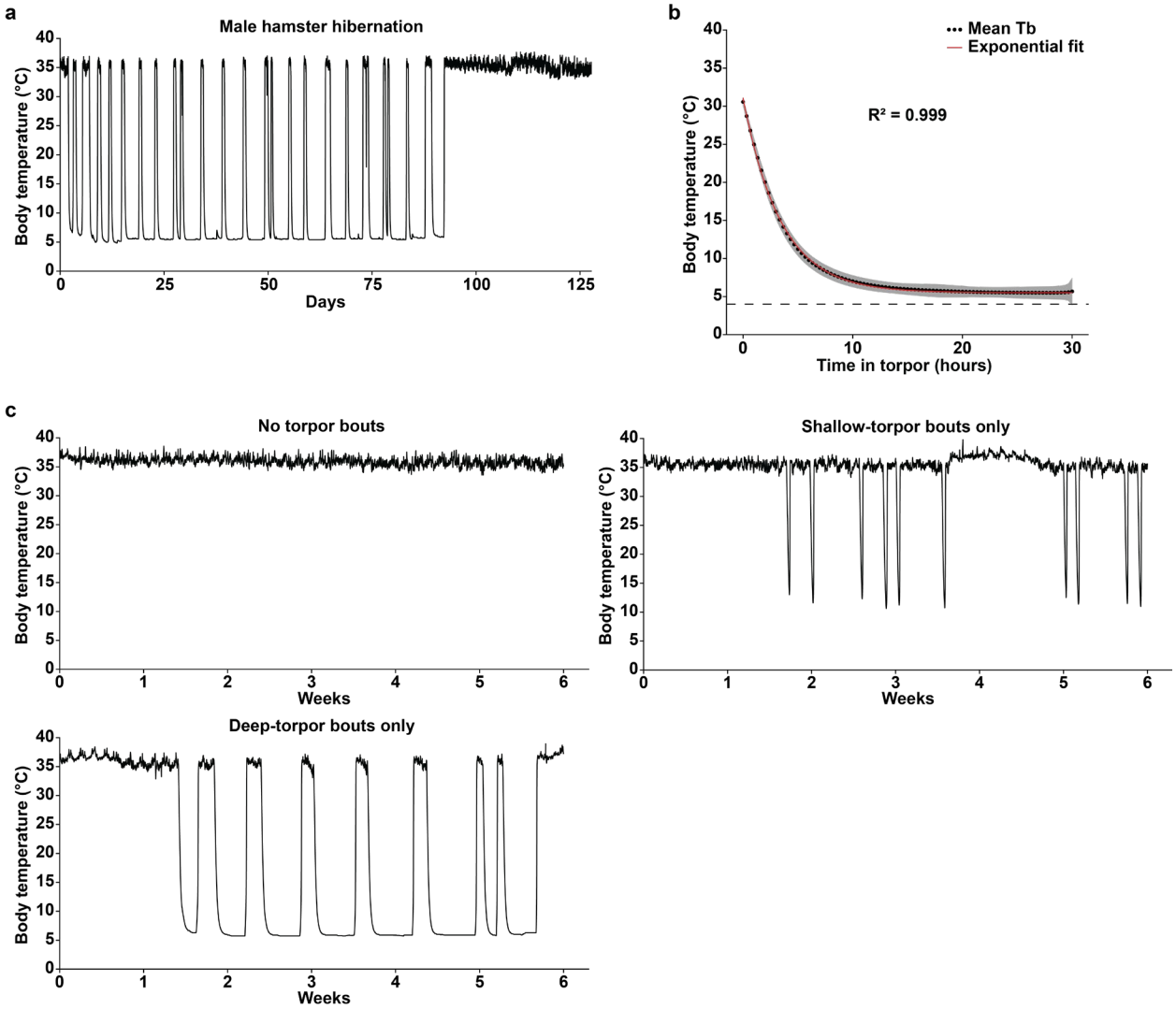

955

956 **Extended Data Fig. 1 Core body temperature dynamics during hibernation.**

957 **a**, Representative core body temperature trace from a male hamster across its

958 hibernation season.

959 **b**, Initial T_b decreases during torpor onset follow an exponential decay (animals = 188,

960 torpor bouts = 1262).

961 **c**, Body temperature traces from three animals within a 6-week observation period,

962 demonstrating the range of T_b changes.

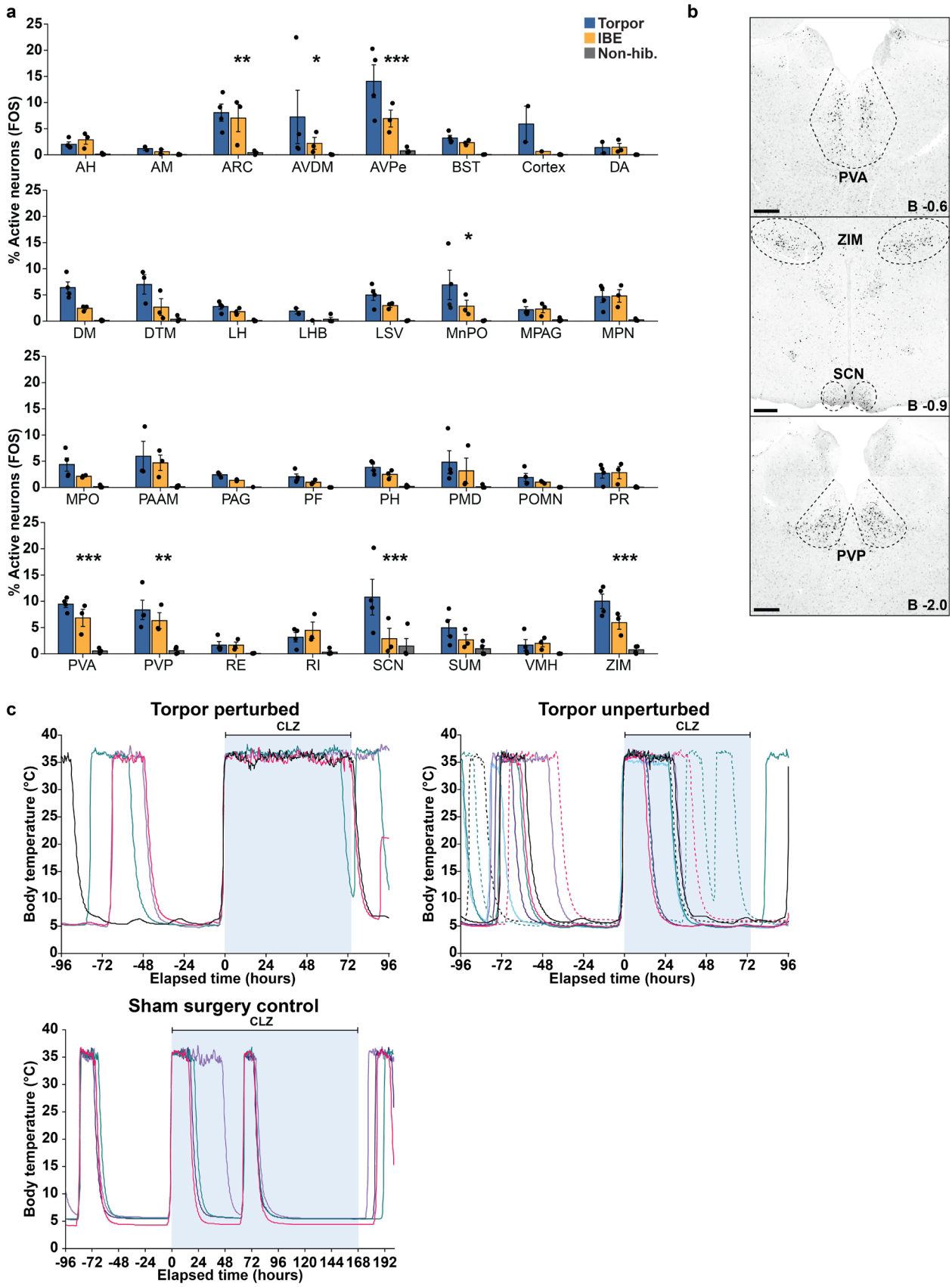
a
Torpor
IBE
Non-hib.
% Active neurons (FOS)
AH
AM
ARC
AVDM
AVPe
BST
Cortex
DA
DM
DTM
LH
LHB
LSV
MnPO
MPAG
MPN
MPO
PAAM
PAG
PF
PH
PMD
POMN
PR
PVA
PVP
RE
RI
SCN
SUM
VMH
ZIM
b
PVA
B -0.6
ZIM
SCN
B -0.9
PVP
B -2.0
c
Torpor perturbed
Torpor unperturbed
Sham surgery control
CLZ
Body temperature (°C)
Elapsed time (hours)

963

964 **Extended Data Fig. 2 Hibernation-associated neuronal activity and disruption of**
965 **torpor entry during targeted silencing.**
966 **a**, Bar plots showing the percentage of FOS-expressing neurons across all surveyed
967 regions (n = 32) and hibernation stages (non-hibernating = 3 animals, IBE = 3 animals,
968 torpor = 4 animals, p-adjusted < 0.05, **p-adjusted < 0.01, ***p-adjusted < 0.001). Data
969 presented as mean ± s.e.m.
970 **b**, Representative FOS immunostaining images of an animal in torpor. The top four deep
971 torpor-active regions after the AVPe are shown: Paraventricular thalamic nucleus anterior
972 (PVA), zona incerta (ZIM), suprachiasmatic nucleus (SCN), and paraventricular thalamic
973 nucleus posterior (PVP).
974 **c**, Hibernating hamsters (n = 13) were injected with AAV-hSyn-hM4D(Gi)-mCherry,
975 targeting different areas of the anterior hypothalamus. After recovery of DT bouts,
976 clozapine (CLZ, 5 mg/kg) was administered via drinking water. Hamster core body
977 temperature traces are shown, demonstrating CLZ-dependent perturbation of torpor
978 activity in a subset of animals (n = 4) while torpor entry remains unaffected in other
979 animals (n = 9).

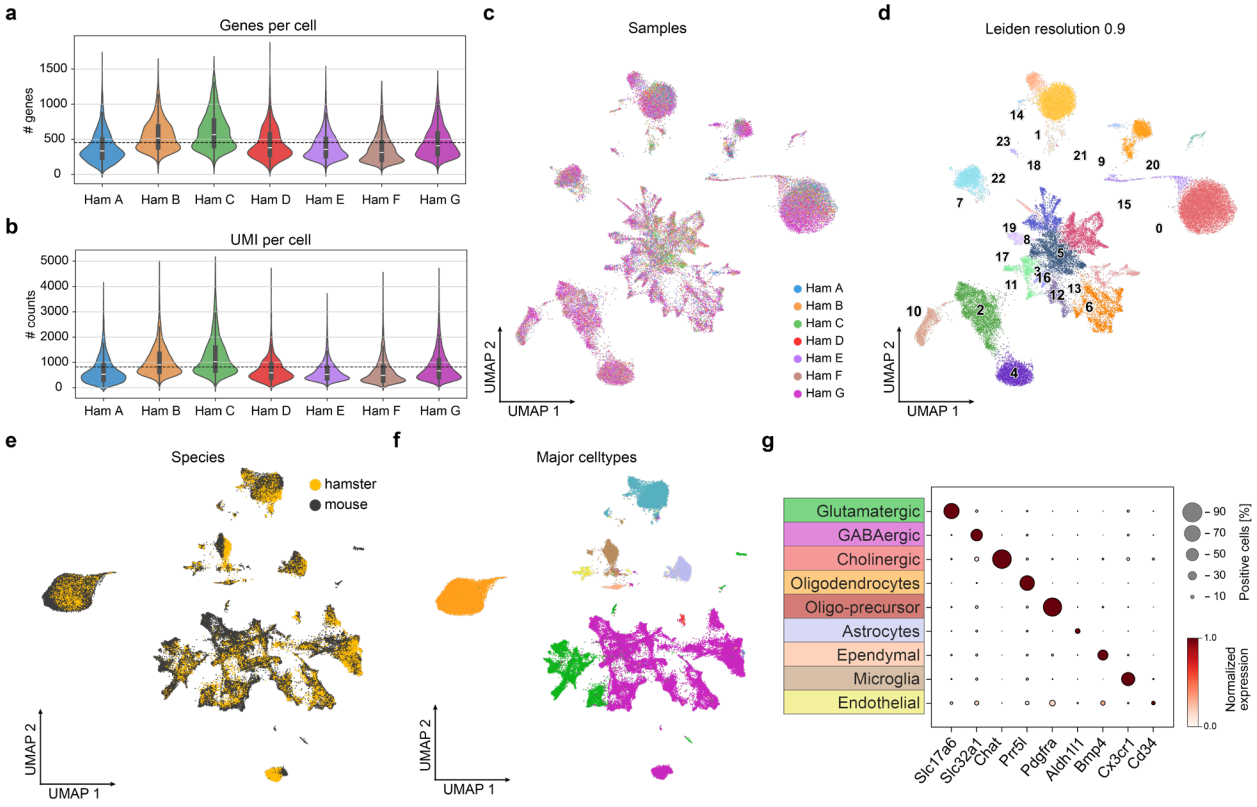

Extended Data Fig. 3 snRNA-seq analysis of hamster and mouse POA and separation of major neuronal and non-neuronal cell types.

Our snRNA-seq and snATAC-seq data from hamster POA samples were first aligned with the mouse POA multiome dataset from Kaplan et. al[75], separating major neuronal and non-neuronal cell types from both datasets.

a,**b**, Violin plots showing the number of detected genes (**a**) and unique transcripts (UMIs) (**b**) per cell in each hamster snRNA-seq sample.

c,**d**, UMAP plots showing 43,243 nuclei across 7 hamster samples and their Leiden clustering.

e,**f**, UMAP plots showing an integrated dataset containing 45,553 hamster and mouse nuclei, and their separation into major cell types.

992 **g**, Dot plot showing the expression of select gene markers of each major neuronal and
993 non-neuronal cell type. Color indicates gene expression scaled across different cell types.
994 Circle size indicates the percentage of cells expressing each marker gene.

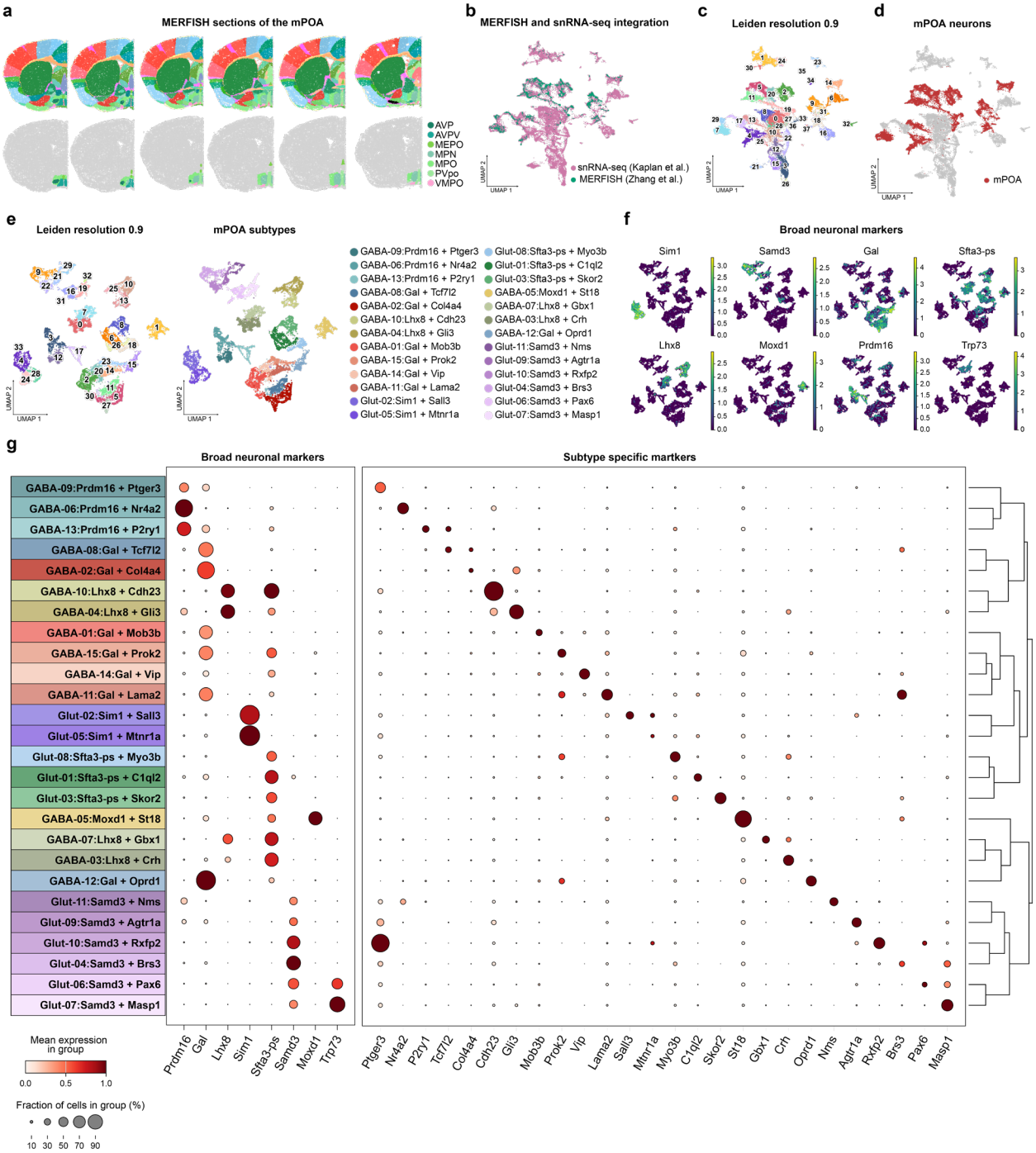

Extended Data Fig. 4 Creation of a mouse mPOA reference transcriptomic dataset. A mouse reference transcriptomic dataset restricted to cell types in our target regions – the medial and median POA (mPOA) – was generated. To this end, mouse spatial transcriptomic data (MERFISH)[76] was subset to only include neurons found in the mPOA

1000 and co-clustered with mouse neuronal snRNA-seq populations from Extended Data Fig.
1001 3f, g, enabling the annotation of 15 GABAergic and 11 glutamatergic mPOA neuronal
1002 populations in the mouse snRNA-seq dataset.
1003 **a**, Coronal brain sections indicating subregions of the mPOA. MERFISH data was subset
1004 to only include neurons within the indicated mPOA regions.
1005 **b**, UMAP plot showing the integrated MERFISH mPOA and mouse snRNA-seq dataset.
1006 **c**,**d**, UMAP plot showing Leiden clustering (**c**) and regional annotation (**d**) of the integrated
1007 MERFISH mPOA and mouse snRNA-seq dataset.
1008 **e**, UMAP plot of only mPOA neurons from (d) colored by Leiden cluster number (left), or
1009 annotated clusters (right). Annotation comprises cell class (Glut = glutamatergic, GABA
1010 = GABAergic), followed by key marker genes. These cells comprise the mouse mPOA
1011 reference transcriptomic dataset.
1012 **f**, UMAP plot showing expression of select marker genes in mouse mPOA.
1013 **g**, Dot plot showing the expression of cell-type-specific marker genes in mouse mPOA.

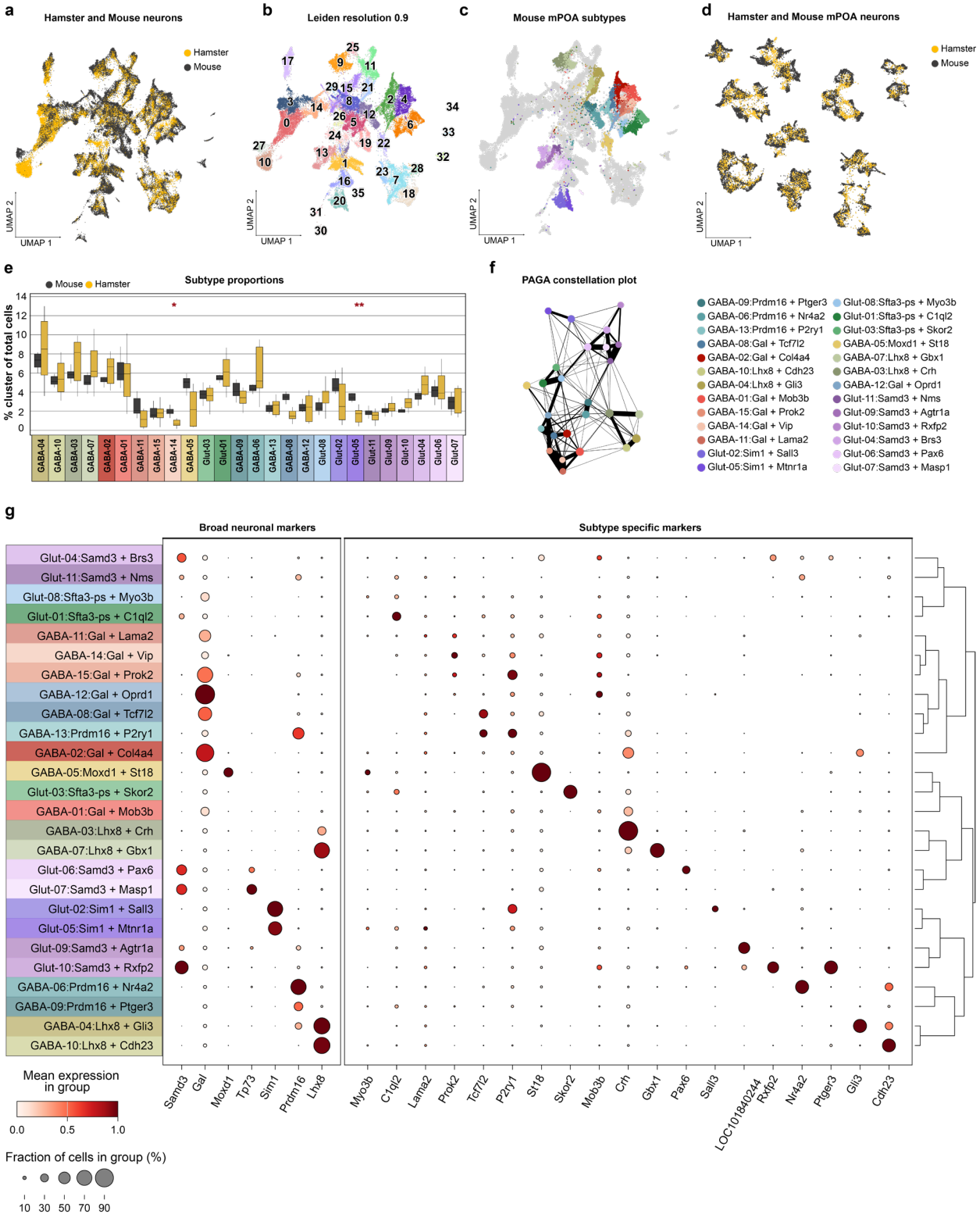

Extended Data Fig. 5 Integration of hamster snRNA-seq with the mouse mPOA reference transcriptomic dataset.

1017 Leveraging the annotations from the mouse mPOA reference transcriptomic dataset
1018 (Extended Data Fig. 4), we annotated neurons from the hamster POA snRNA-seq dataset
1019 to generate the final cross-species atlas.
1020 **a**,**b**, UMAP plot showing integrated hamster and mouse neuronal snRNA-seq data,
1021 colored by species of origin (**a**), or Leiden cluster (**b**).
1022 **c**, UMAP plot highlighting the location of mouse mPOA neurons, colored based on
1023 clusters from the mouse mPOA reference transcriptomic dataset.
1024 **d**, UMAP plot as in Fig. 3 displaying all mouse and hamster mPOA neurons from the
1025 snRNA-seq dataset, colored by the clusters defined in the mouse mPOA reference
1026 transcriptomic dataset.
1027 **e**, Relative abundance of each cell type in the mouse and hamster POA dataset. Three
1028 cell types show significant differences in abundance (* $P < 0.05$, ** $P < 0.01$, Mann-
1029 Whitney U test).
1030 **f**, Constellation plot showing the relationships between subtypes based on their latent
1031 space.
1032 **g**, Dot plot showing the expression of cell-type-specific marker genes for hamster
1033 neurons.

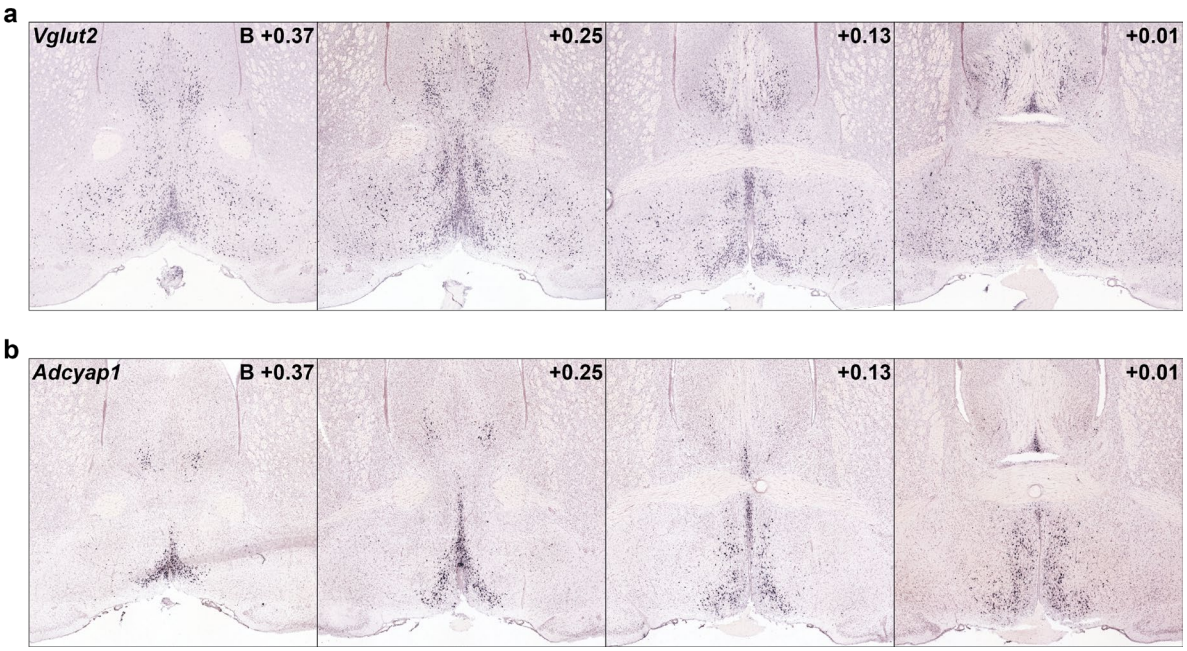

1034

1035 **Extended Data Fig. 6 Anatomical distribution of mouse FIT-associated neurons.**

1036 **a**,**b**, Example coronal sections of the mouse brain containing the anterior POA, showing

1037 ISH signal for marker genes *Slc17a6/Vglut2* (A) and *Adycap1* (B). Data from mouse.brain-

1038 map.org[103].

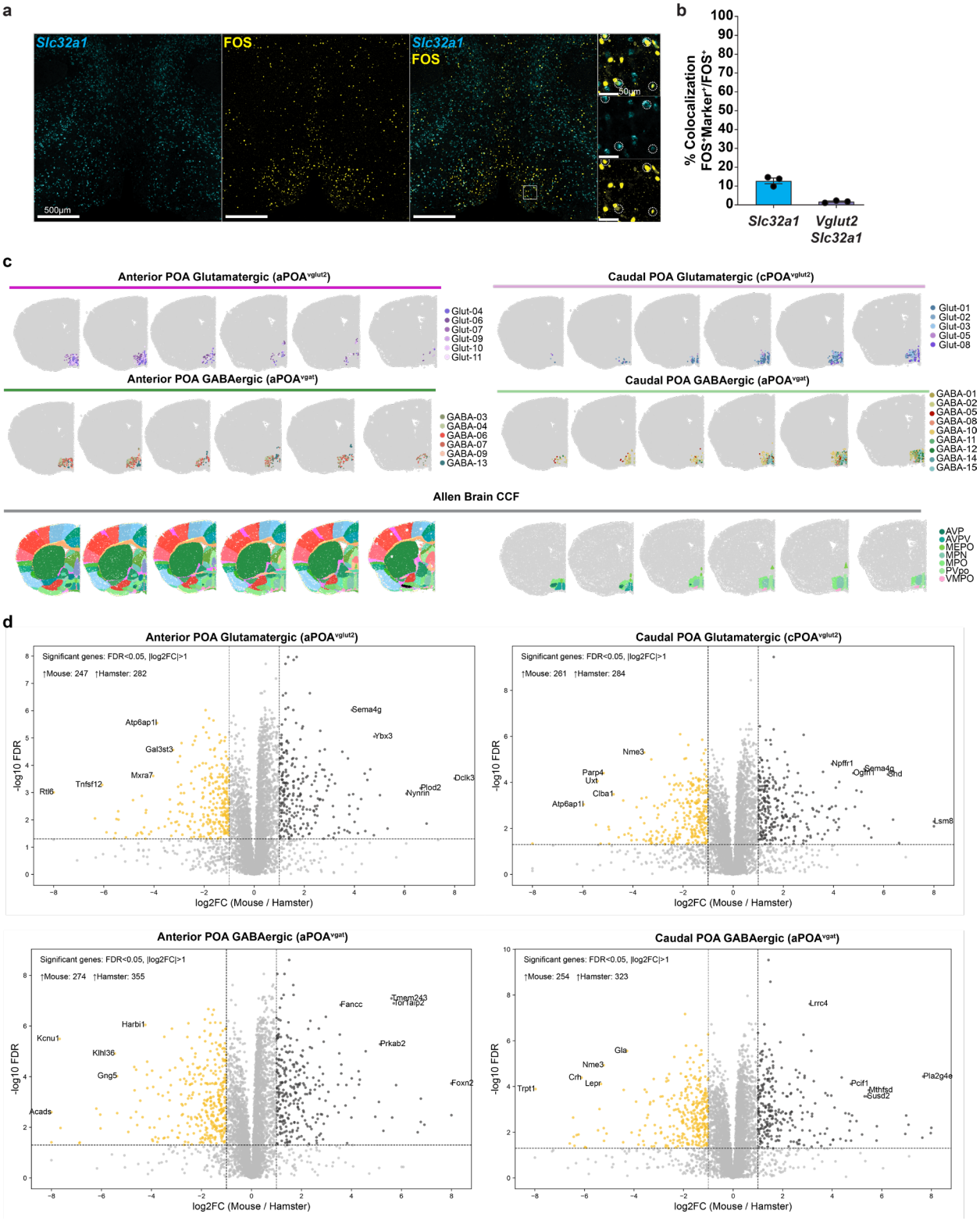
a
Slc32a1
FOS
Slc32a1
FOS
500μm
50μm
b
% Colocalization
FOS+Marker+/FOS+
Slc32a1
Vglut2
Slc32a1
c
Anterior POA Glutamatergic (aPOAvglut2)
Glut-04
Glut-06
Glut-07
Glut-09
Glut-10
Glut-11
Caudal POA Glutamatergic (cPOAvglut2)
Glut-01
Glut-02
Glut-03
Glut-05
Glut-08
Anterior POA GABAergic (aPOAvgat)
GABA-03
GABA-04
GABA-06
GABA-07
GABA-09
GABA-13
Caudal POA GABAergic (aPOAvgat)
GABA-01
GABA-02
GABA-05
GABA-08
GABA-10
GABA-11
GABA-12
GABA-14
GABA-15
Allen Brain CCF
AVP
AVPV
MEPO
MPN
MPO
PVpo
VMPO
d
Anterior POA Glutamatergic (aPOAvglut2)
Significant genes: FDR<0.05, |log2FC|>1
↑Mouse: 247 ↑Hamster: 282
Sema4g
Ybx3
Atp6ap1l
Gal3st3
Mxra7
Tnfsf12
Rtl6
Plod2
Nynrin
Dclk3
-log10 FDR
log2FC (Mouse / Hamster)
Caudal POA Glutamatergic (cPOAvglut2)
Significant genes: FDR<0.05, |log2FC|>1
↑Mouse: 261 ↑Hamster: 284
Nme3
Parp4
Uxt
Clba1
Atp6ap1l
Npffr1
Ogfrl1
Sema4g
Snd
Lsm8
-log10 FDR
log2FC (Mouse / Hamster)
Anterior POA GABAergic (aPOAvgat)
Significant genes: FDR<0.05, |log2FC|>1
↑Mouse: 274 ↑Hamster: 355
Fancc
Tmem243
Rorf1alp2
Harbi1
Kcnu1
Klhl36
Gng5
Prkab2
Foxn2
Acads
-log10 FDR
log2FC (Mouse / Hamster)
Caudal POA GABAergic (aPOAvgat)
Significant genes: FDR<0.05, |log2FC|>1
↑Mouse: 254 ↑Hamster: 323
Lrrc4
Gla
Nme3
Crh
Lepr
Trpt1
Pcif1
Mthfsd
Gusd2
Pla2g4e
-log10 FDR
log2FC (Mouse / Hamster)

1039

1040 **Extended Data Fig. 7 Marker expression of DT-active neurons; anatomical**
1041 **localization and cross-species differential gene expression of POA neuronal**
1042 **populations.**

1043 **a**, Example coronal sections showing the aPOA of a Syrian hamster collected during DT
1044 onset. Immunofluorescent staining against FOS indicates the location of active neurons
1045 (yellow), whereas ISH indicates the expression of the marker gene *Slc32a1* (*Vgat*). High-
1046 magnification images are shown as insets with example FOS+ *Slc32a1*+ cells circled.

1047 **b**, Quantification of the fraction of FOS+ neurons during torpor that express *Slc32a1*
1048 (12.8% ± 1.5, animals = 3) and dual-expressing *Slc17a6/Slc32a1* (1.8% ± 0.3, n = 3)
1049 neurons. Data presented as mean ± s.e.m.

1050 **c**, MERFISH plot showing the spatial distribution of neuronal subtypes in the mouse POA
1051 separated by their major cell types and anatomical location.

1052 **d**, Differential gene expression between hamster and mouse neurons across the four
1053 major neuron groups.

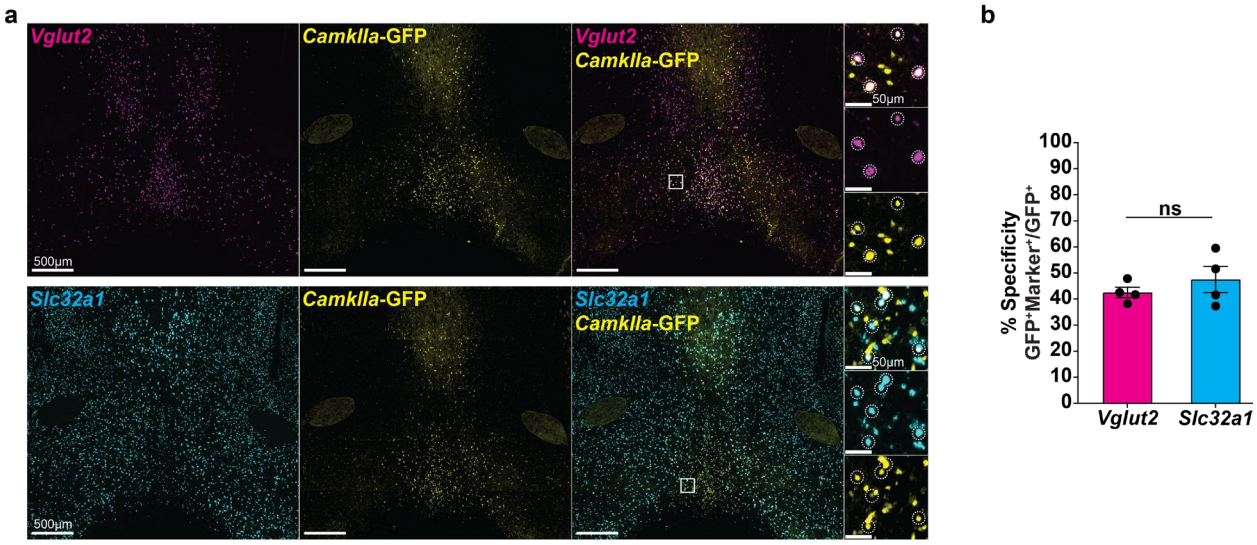

1054

1055 **Extended Data Fig. 8 *CamkIIa* promoter-based AAVs lack specificity for**

1056 **glutamatergic neurons in the hamster aPOA.**

1057 Hamsters (n = 4) were stereotaxically administered AAV8-CamkIIa-GFP and harvested

1058 ~2 weeks later for immunostaining and ISH.

1059 **a**, Example coronal sections showing the hamster POA comprising AVPe, MPA, and

1060 MnPO. Immunofluorescent staining against GFP indicates the location of virally labeled

1061 cells (yellow), whereas ISH indicates the expression of genes *Slc17a6* (*Vglut2; magenta*)

1062 and *Slc32a1 (Vgat; cyan)*. High-magnification images are shown on the right with

1063 example GFP+ *Marker*+ cells circled.

1064 **b**, Quantification of the fraction of AAV-CamkIIa-GFP+ neurons that express *Slc17a6*

1065 (42.6% ± 2.0, animals = 4), and *Slc32a1* (47.5 ± 5.0%, animals = 4). Data presented as

1066 mean ± s.e.m.

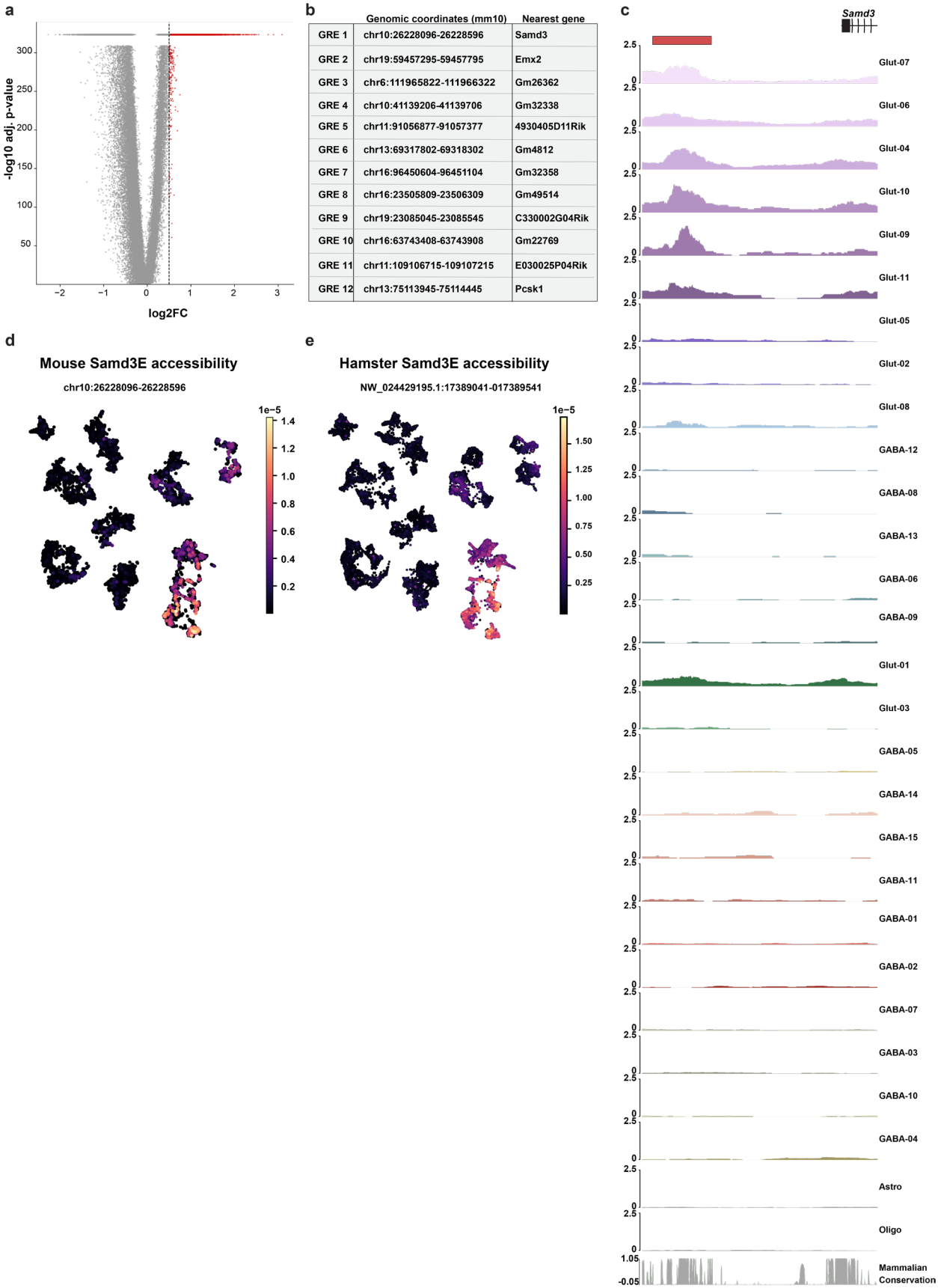

	Genomic coordinates (mm10)	Nearest gene
GRE 1	chr10:26228096-26228596	Samd3
GRE 2	chr19:59457295-59457795	Emx2
GRE 3	chr6:111965822-111966322	Gm26362
GRE 4	chr10:41139206-41139706	Gm32338
GRE 5	chr11:91056877-91057377	4930405D11Rik
GRE 6	chr13:69317802-69318302	Gm4812
GRE 7	chr16:96450604-96451104	Gm32358
GRE 8	chr16:23505809-23506309	Gm49514
GRE 9	chr19:23085045-23085545	C330002G04Rik
GRE 10	chr16:63743408-63743908	Gm22769
GRE 11	chr11:109106715-109107215	E030025P04Rik
GRE 12	chr13:75113945-75114445	Pcsk1

1067

1068 **Extended Data Fig. 9 snATAC-seq analysis reveals *Samd3E* as tool to target POA**
1069 **neurons.**

1070 **a**, Differential accessibility analyses of genomic elements in aPOA^{Vglut2} neurons vs. all
1071 other neurons in mice; top regions (log2FC > 0.5) are marked in red for further analysis.

1072 **b**, Genomic location and nearest gene of the top candidate putative GREs.

1073 **c**, ATAC-seq genome browser tracks (normalized counts per location) of individual mouse
1074 neuronal subtypes showing the mouse *Samd3*-proximal putative GRE (*Samd3E,* red
1075 box), with accompanying sequence conservation below.

1076 **d**,**e**, UMAP feature plots depicting *Samd3E* accessibility in the indicated species.

1077 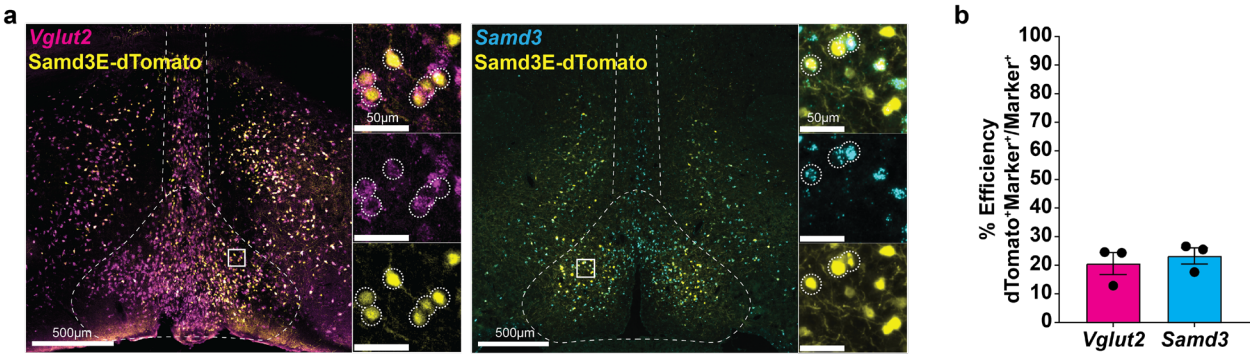

1078 **Extended Data Fig. 10 Samd3E-AAV transduction efficiency.**

1079 **a**, Efficiency of targeting aPOA^{Vglut2} and aPOA^{Samd3} neurons with AAV8-Samd3E-
1080 dTomato. Syrian hamsters (n = 3) were injected with AAV8-Samd3E-dTomato.
1081 Immunofluorescent staining against dTomato was used to identify virally labeled cells
1082 (yellow), whereas ISH indicates the expression of the marker gene *Slc17a6* (*Vglut2*,
1083 magenta) and *Samd3* (cyan), as in Fig. 4g.

1084 **b**, Quantification of the fraction of *Slc17a6*+ cells that also express dTomato+ (20.6 ±
1085 3.9%, animals = 3) and *Samd3*+ cells that also express dTomato+ (23.3 ± 2.8%, animals
1086 = 3). Given limited viral spread, this quantification was limited to the area of viral
1087 expression within the aPOA. These results indicate that AAV8-Samd3E-dTomato
1088 achieves high specificity and modest efficiency for targeting aPOA^{Vglut2} and aPOA^{Samd3}
1089 neurons.

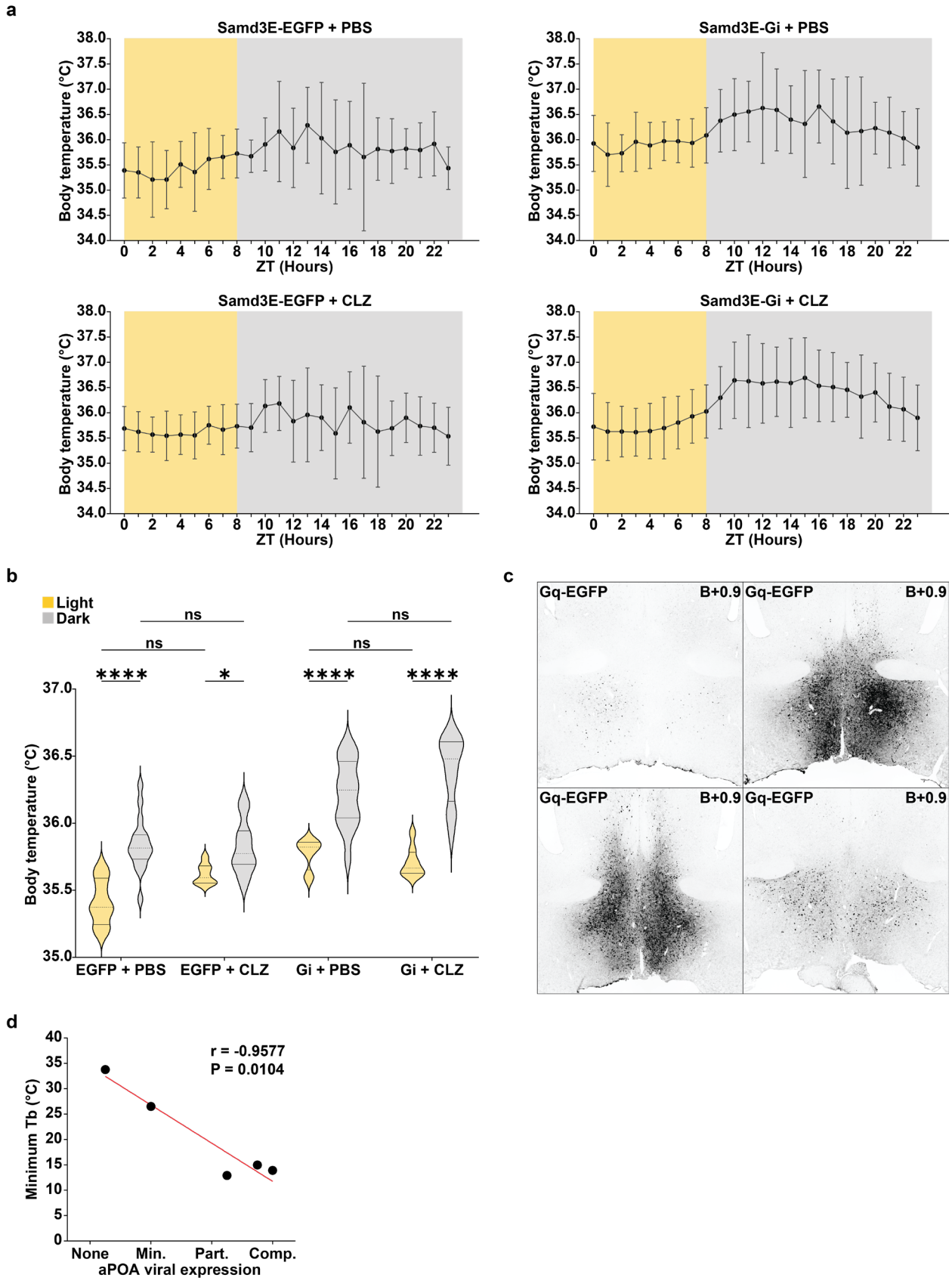
a
Samd3E-EGFP + PBS
Samd3E-Gi + PBS
Samd3E-EGFP + CLZ
Samd3E-Gi + CLZ
Body temperature (°C)
ZT (Hours)
b
Light
Dark
ns
****
*
EGFP + PBS
EGFP + CLZ
Gi + PBS
Gi + CLZ
c
Gq-EGFP
B+0.9
d
r = -0.9577
P = 0.0104
Minimum Tb (°C)
None
Min.
Part.
Comp.
aPOA viral expression

1090

1091 **Extended Data Fig. 11 Circadian T_b patterns and correlation between viral aPOA**
1092 **expression and T_b decrease.**

1093 **a**, Circadian fluctuation of T_b in Samd3E-EGFP- and Samd3E-Gi-DREADD-injected
1094 hamsters following administration of CLZ (5 mg/kg) or control PBS. Light and dark cycle
1095 phases are represented by yellow and grey, respectively. Data presented as mean ± s.d.
1096 of core body temperatures during each hour.

1097 **b**, Violin plot quantification of body temperature range between light (yellow) and dark
1098 (grey) phases of Samd3E-EGFP- (n = 5 animals) or Samd3E-Gi-DREADD-injected
1099 animals (n = 12) following CLZ or control PBS administration (Tukey's multiple
1100 comparisons test; *P-adjusted < 0.05, ****P-adjusted < 0.0001, ns = not significant P >
1101 0.05).

1102 **c**, Immunofluorescence images in the aPOA of additional Samd3E-Gq-DREADD-EGFP-
1103 injected animals.

1104 **d**, Correlation between minimum T_b reached following CLZ administration and viral
1105 expression within the aPOA (n = 5 animals, r = -0.95, P = 0.01).

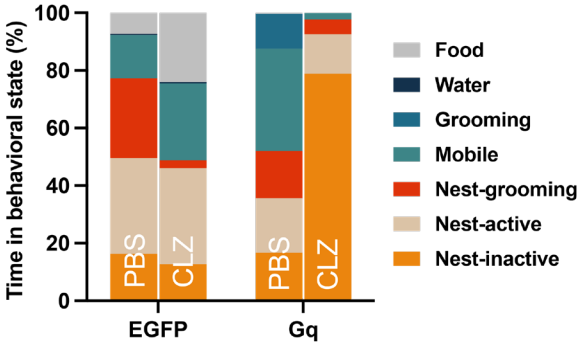

1106

1107 **Extended Data Fig. 12 Changes in behavioral repertoire after aPOA^{Vglut2} neuronal**

1108 **activation.**

1109 Percentage of time in behavioral states over a 10 min observation window post-injection

1110 with PBS or CLZ across all hamsters injected with AAV-Samd3E-EGFP-P2A-

1111 Synaptophysin-mRuby (n = 3) and AAV-Samd3E-hM3D(Gq)-nlsGFP (n=6).

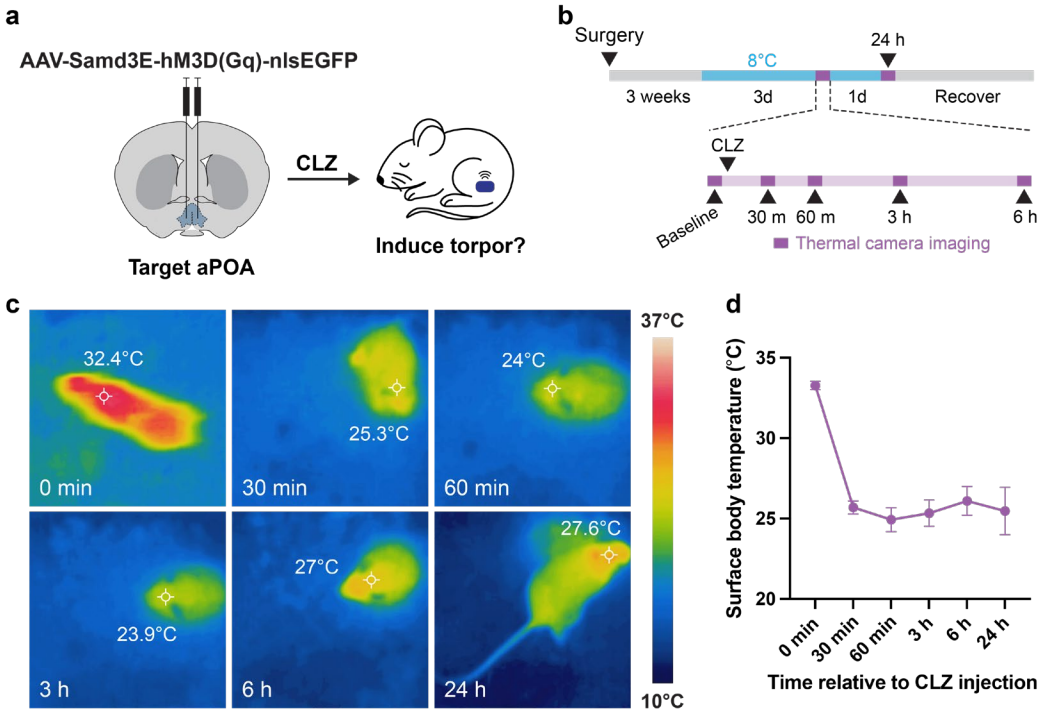

Extended Data Fig. 13 Stimulation of aPOA^{Vglut2} neurons in mice and resulting body temperature change.

a, Schematic of experimental design.

b, Timeline of experiment and analysis. Mice were acclimated to 8°C for 3 days before injection with CLZ (5 mg/kg) and imaged with a thermal camera at baseline, 30 min, 60 min, 3 hours, 6 hours, and 24 hours post injection at 8°C.

c, Representative thermographic images obtained by chemogenetic stimulation of aPOA^{Vglut2} neurons.

d, Surface body temperature before (0 min) and after (30 min to 24 h) CLZ injection (n=7 mice). Data are presented as mean ± s.e.m.

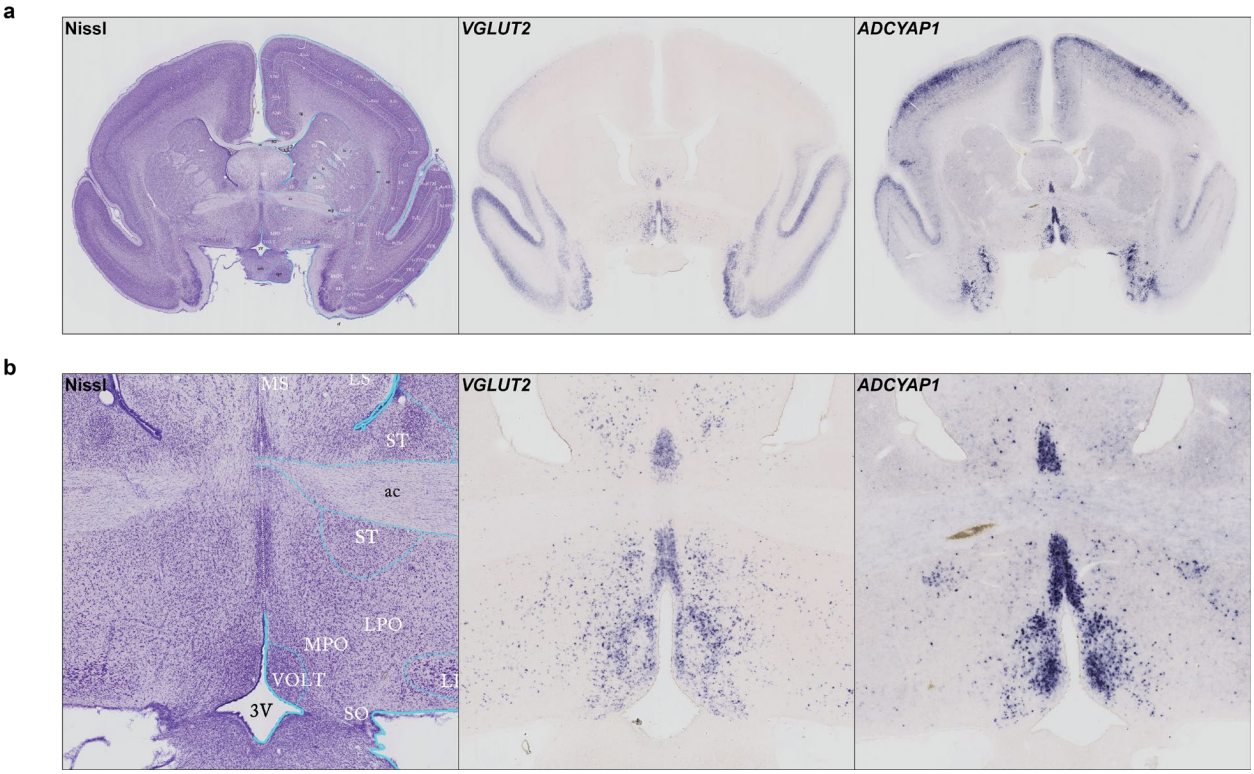

Extended Data Fig. 14 *In situ* hybridization for marker of torpor-associated genes in marmosets.

a, Example coronal sections of the marmoset brain containing the anterior POA showing ISH signal for marker genes *Slc17a6/Vglut2* and *Adycap1*.

b, Higher resolution images from (A) displaying the anterior POA. Data from https://gene-atlas.brainminds.jp/[90–92].